Atmospheric
Chemistry
and Physics
Discussions

Iron (Fe) speciation in size-fractionated aerosol particles in the Pacific Ocean: The role of organic complexation of Fe with humic-like substances in controlling Fe solubility

Kohei Sakata[1], Minako Kurisu[2], Yasuo Takeichi[3], Aya Sakaguchi[4], Hiroshi Tanimoto[1], Yusuke
5 Tamenori[5], Atsushi Matsuki[6], Yoshio Takahashi[3,7]

[1]Center for Global Environmental Research, National Institute for Environmental Studies, 16-2 Onogawa, Tsukuba, Ibaraki 305-8506, Japan.
[2]Research Institute for Global Change, Japan Agency for Marine-Earth Science and Technology, 2-15, Natsushima-cho, Yokosuka, Kanagawa 237-0061, Japan.
10 [3]Institute of Material Structure Science, High-Energy Accelerator Research Organization, Tsukuba, Ibaraki 305-0801, Japan.
[4]Faculty of Pure and Applied Science, University of Tsukuba, 1-1-1 Tennodai, Tsukuba, Ibaraki 305-8577, Japan.
[5]Japan Synchrotron Radiation Research Institute/SPring-8, 1-1-1 Kouto, Sayo, Hyogo 679-5198, Japan.
[6]Institeu of Nature and Environmental Technology, Kanazawa University, Kakuma, Knazawa, Ishikawa 920-1192, Japan.
[7]Graduate School of Science, The University of Tokyo, 7-3-1 Hongo, Bunkyo-ku, Tokyo 113-0033, Japan.

15 *Correspondence to*: Kohei Sakata (sakata.kohei@nies.go.jp)

Atmospheric
Chemistry
and Physics
Discussions

Abstract.

Atmospheric deposition is one of the dominant sources of dissolved Fe on the ocean surface. Atmospheric processes are recognized as controlling fractional Fe solubility (Fe_{sol}%) in marine aerosol particles, but the impact of these processes on

20   Fe_{sol}% remains unclear. One of the reasons for this is the lack of field observations focusing on the relationship between Fe_{sol}% and Fe species in the marine aerosol particles. In particular, the effects of organic ligands on the Fe_{sol}% have not been well investigated through observational studies. In this study, Fe species in size-fractionated aerosol particles in the Pacific Ocean were determined by X-ray absorption fine structure (XAFS) spectroscopy. The internal mixing states of Fe with organic carbons were investigated using scanning transmission X-ray microscopy (STXM). The effects of atmospheric processes on

25   Fe_{sol}% in the marine aerosol particles were investigated based on these speciation results. Iron in size-fractionated aerosol particles was mainly derived from mineral dust regardless of aerosol diameter because the enrichment factor of Fe was almost 1 in both coarse ($PM_{1.3-10.2}$) and fine aerosol particles ($PM_{1.3}$). About 80% of total Fe (insoluble + labile Fe) was present in coarse aerosol particles ($PM_{1.3-10.2}$), whereas labile Fe was mainly present in fine aerosol particles ($PM_{1.3}$). The Fe_{sol}% in $PM_{1.3-10.2}$ was not well increased (2.56±2.53 %, 0.00–8.50 %, n =20) by the atmospheric processes because mineral dust was not

30   acidified beyond the buffer capacity of calcite. By contrast, mineral dust in $PM_{1.3}$ was acidified beyond the buffer capacity of calcite. As a result, Fe_{sol}% in $PM_{1.3}$ (0.202–64.7 %, n=10) is an order of magnitude higher than those in $PM_{1.3-10.2}$. The $PM_{1.3}$ contained ferric organic complexes with humic-like substances (Fe(III)-HULIS, but not included Fe-oxalate complexes), of which abundance correlated with Fe_{sol}%. The Fe(III)-HULIS was formed during transport in the Pacific Ocean since the Fe(III)-HULIS was not found in aerosol particles in Beijing and Japan. The pH estimations of mineral dust in $PM_{1.3}$ revealed

35   that Fe was solubilized by proton-promoted dissolution under highly acidic conditions (pH < 3.0), whereas Fe(III)-HULIS was stabilized under moderately acidic conditions (pH: 3.0–6.0). Since the observed labile Fe concentration could not be reproduced by proton-promoted dissolution under moderately acidic conditions, the pH of mineral dust was increased after proton-promoted dissolution. The cloud process in the marine atmosphere increased the pH of mineral dust because the dust particles were covered with organic carbons and Na. At this stage, the precipitation of ferrihydrite was suppressed by Fe(III)-

40   HULIS because of its high water solubility. Thus, the organic complexation of Fe with HULIS plays a significant role in the stabilization of Fe initially solubilized by proton-promoted dissolution.

1. Introduction

Primary production on the ocean surface is limited by the depletion of dissolved iron (Fe, Martin and Fitzwater, 1988; Jickells et al., 2005; Baker et al., 2016, 2021; Mahowald et al., 2018; Meskhidze et al., 2019). The fertilization of Fe in the surface ocean has the potential to regulate global climate systems via the uptake of atmospheric carbon dioxides (CO_2) in the surface seawater. Dissolved iron must be supplied to activate biological activity because microorganisms utilize dissolved Fe as micronutrients (Boyd et al., 2007; Moore et al., 2013; Mahowald et al., 2018). Atmospheric deposition of Fe in mineral dust is one of the dominant sources of dissolved Fe on the ocean surface (Jickells et al., 2005; Baker et al., 2016, 2021; Mahowald et al., 2018; Meskhidze et al., 2019). However, fractional Fe solubility ($Fe_{sol}\% = (labile~Fe/total~Fe) \times 100$) in mineral dust in source regions is usually less than 1.0% because Fe in mineral dust is typically present as insoluble species (e.g., Fe in aluminosilicates and Fe (hydr)oxides). In contrast, a wide range of $Fe_{sol}\%$ in marine aerosol particles (0.1–90%) has been reported by previous observational studies (Buck et al., 2006; 2010; 2013, Baker and Jickells, 2006; Bakers et al., 2016, 2021; Chance et al., 2015; Kurisu et al., 2021). One of the reasons for high $Fe_{sol}\%$ in the marine aerosol particles is pyrogenic Fe with high $Fe_{sol}\%$ (up to 80%, Schroth et al., 2009; Takahashi et al., 2013; Kurisu et al., 2016; 2019, 2021; Conway et al., 2019). It seems that the variation of $Fe_{sol}\%$ in marine aerosol particles can be explained by a binary mixing system of mineral dust and anthropogenic aerosols if the $Fe_{sol}\%$ of these components at the time of emission is known. However, it is difficult to explain the variation of $Fe_{sol}\%$ in the marine aerosol particles by the mixing system because atmospheric processes during transport affect $Fe_{sol}\%$ of mineral dust and anthropogenic Fe.

Atmospheric processes of Fe are described as proton-promoted, ligand-promoted, and photo-reductive Fe dissolutions (Bakers et al., 2016, 2021; Mahowald et al., 2018; Meskhidze et al., 2019 and references therein). The proton-promoted Fe dissolution is mainly driven by aerosol acidifications (Desboufs et al., 1999; Mackie et al., 2005; Cwiertny et al., 2008; Shi et al., 2009, 2011, 2015; Maters et al., 2016). As a proof of the acidification of Fe-bearing particles, the single-particle analysis revealed that internal mixing of Fe with sulfate, nitrate, and chloride were identified in the atmosphere (Sullivan et al., 2007; Moffet et al., 2012; Fitzgerald et al., 2015; Li et al., 2017), but these analytical techniques could not mention direct relationships of internal mixing state with aerosol pH and $Fe_{sol}\%$. Therefore, aerosol pH was usually estimated by using thermodynamic model calculations (e.g., E-AIM and ISOROPPIA). The Fe dissolution from aerosol particles is enhanced in the wet aerosol phase with highly acidic conditions (pH < 3.0, Longo et al., 2016; Fang et al., 2017; Tao and Murphy, 2019). However, calculated pH by the thermodynamic models does not necessarily reflect the pH of the mineral dust. One of the reasons is that the calculated result is the pH of the main component of the marine aerosols (e.g., sulfate aerosols and sea spray aerosols), which were usually externally mixed with Fe-bearing particles. Another reason is that the aerosol pH of proton-promoted dissolution cannot uniquely determine the aerosol pH since the Fe-bearing particles may go through pH cycles according to evaporation-condensation cycles. Therefore, it is preferred that the average pH of Fe-bearing particles for proton-promoted dissolution are evaluated based on $Fe_{sol}\%$ and/or labile (L-Fe) concentrations.

In the case of ligand-promoted and photo-reductive Fe dissolutions, organic ligands play a significant role in the
enhancement of $Fe_{sol}\%$ in marine aerosol particles. The formation of organic complexes on the surface of Fe-oxides destabilizes
the Fe−O bond (Wang et al., 2017). The complexation of L-Fe with organic complexes decreases a saturation index of Fe in
aerosol liquid water (ALW). The photoreduction of Fe(III)-organic complexes also decreases the saturation index of Fe(III) in
the ALW because of the formation of Fe(II) (Chen and Grassian, 2013). As a result of these interactions of Fe with organic
ligands, the dissolution of Fe-bearing particles is promoted. It is considered that oxalate is an important ligand in aerosol
particles because oxalate is ubiquitously present in aerosol particles. However, the mass fraction of oxalate in water-soluble
organic carbon (WSOC) is usually lower than 10% (Bikkina et al., 2015; Kawamura and Bikkina, 2016). In contrast, more
than half of WSOC is present as humic-like substances (HULIS), which are also considered to affects $Fe_{sol}\%$ in aerosol particles
(Wozniak et al., 2013, 2015; Al-Abdleh 2015). In addition, siderophores have been detected in aerosol, rainwater, and cloud
water (Cheize et al., 2012; Sullivan et al., 2012; Vinatier et al., 2016). The siderophore has higher stability constant with Fe
than oxalate, and the Fe-siderophore complexes have high water solubility (Cheize et al., 2012). Recently, the Fe(III)-dextrans
as Fe(III)-organic complexes have been detected in $PM_{2.5}$ collected in Colorado, USA (Salazar et al., 2020). The formation of
Fe-organic complexes may suppress the precipitation of nano-ferrihydrite when the acidified aerosol particles with high $Fe_{sol}\%$
encounters high pH solution because these Fe-organic complexes have higher water solubility than inorganic Fe under wide
pH range. However, the effects of Fe(III)-organic complexes of HULIS and siderophore in atmospheric samples on $Fe_{sol}\%$
have not been well investigated through the field observations of marine aerosol particles.

In this study, Fe species in size-fractionated aerosol particles in the Pacific Ocean were determined by X-ray absorption
fine structure (XAFS) spectroscopy to investigate a relationship between Fe species and $Fe_{sol}\%$. The XAFS spectroscopy
provides us the average fraction of Fe species, which can directly compare to $Fe_{sol}\%$. In addition, Al species in several size-
fractionated aerosol particles were determined to evaluate the aging effect of aluminosilicates in the samples. The Al K-edge
X-ray absorption near-edge structure (XANES) spectrum is sensitive to the coordination chemistry of Al (Ildefonse et al.,1998;
Shaw et al., 2009; Hagvall et al., 2015). Furthermore, internal mixing states of Fe with organic carbons (OCs) were investigated
using scanning transmission X-ray microscopy (STXM) to evaluate detailed alteration processes of Fe-bearing particles. Based
on $Fe_{sol}\%$ and speciation results, the average pH required for proton-promoted dissolution (pH_{PPD}) was evaluated using a
conceptual model according to the first-order Fe dissolution. The pH for stabilization of L-Fe species in aerosol particles (pH_{L-Fe}) was evaluated by a geochemical model. If pH_{L-Fe} differs from pH_{PPD}, the L-Fe species are formed under different pH
conditions from the proton-promoted dissolutions. Therefore, differences between pH_{PPD} and pH_{L-Fe} may become an indicator
for pH variation of the Fe-bearing particles. From these results, the role of atmospheric processes in the enhancement of $Fe_{sol}\%$
is discussed in this study.

Atmospheric
Chemistry
and Physics
Discussions

2. Sampling and analytical methods

2.1. Aerosol sampling

Size-fractionated sampling of marine aerosols was conducted on the research cruise of *R/V Hakuho-Maru* (Fig. 1 and Table S1: KH-14-6, Longitudinal cruise of the Western Pacific Ocean, December 2, 2014 to February 26, 2015, GEOTRACES). A high-volume air sampler (MODEL-123SL, Kimoto, Japan) with a Sierra-type cascade impactor (TE-236, Tisch Environmental Inc., USA) was installed on the compass deck of the vessel, located 13 m above sea level. A sampling air flow rate was fixed at 0.566 m^3/min. Wind speed and direction were monitored by a wind-sector control system to prevent the contamination of fly ashes and exhaust gases emitted from the vessel.

Aerosol diameters for each sampling stage (stages 1 to 7) are described in Table S1. Aerosol samples in stages 1 to 4 ($PM_{1.3-10.2} > 1.3$ μm) were defined as coarse aerosol particles, whereas those in stages 5 to 7 were defined as fine aerosol particles ($PM_{1.3} < 1.3$ μm). Aerosol particles in stages 1 to 6 were collected on a custom-built polytetrafluoroethylene (PTFE. about 15 cm^2) filter (Sakata et al. 2018). The filter blanks of Al and Fe were 0.306±0.352 and 0.335±0.340 ng/cm^2, which were corresponding to few pg/m^3. The blank concentrations of Fe and Al were about an order of magnitude lower than the lowest concentration of these elements in our samples. For single particle analysis, aerosol particles were also collected on molybdenum grids with formvar thin film (Mo grid) that fixed on the PTFE filter by a double-face cellulose tape. The PTFE filter was rinsed based on our previous study (Sakata et al., 2018). Aerosol samples in stage 7 were collected on a cellulose filter (Whatman 41, 516 cm^2, GE Healthcare, USA). The filter blank of Al and Fe in the cellulose filter 7.20±3.91 and 16.5±6.27 ng/cm^2, which are corresponded to 2.52 and 5.77 ng/m^3, respectively. Stage 7 was excluded from the discussion because of the high filter background. In this study, sample names are described as the stage number of cascade impactor combined with sampling site (e.g., stage 6 collected in SPO: S6-SPO; Tables S1 and S2).

For comparison, aerosol sampling was performed at Noto Ground-Based Research Observatory (NOTOGRO) located in the coastal region of the Sea of Japan (Suzu, Ishikawa, Japan: 37.4513º N, 137.3589º E). NOTOGRO is located between China and the sampling sites of the WPO (Fig. 1). Size-fractionated aerosol sample influenced by Chinese air mass was collected from February 19 to 26, 2020. In addition, reference materials of Beijing aerosol (NIES CRM 28, Urban dust, Mori et al., 2008) was also employed for comparison of Fe species.

2.2. Total and labile metal concentrations

All sample treatments were conducted in clean booth (Class-100) and an evaporation chamber installed in a Class-10000 clean room. Acid digestion and ultrapure water extractions of aerosol samples were performed to determine total and labile metal concentrations, respectively. Aerosol samples were decomposed by mixed acid (2 mL of 15.2 mol/L HNO_3, 2 mL of 9.3 mol/L HCl, and 1mL of 20 mol/L HF) with heating at 120 °C for 1 day. The mixed acid was evaporated to dryness at 120 °C,

subsequently residues were re-dissolved in 0.15 mol/L HNO₃. Labile metals in aerosol particles were extracted urtrasonically for 30 min with 5 mL of MQ water. The extracted solutions were acidified to 0.15 mol/L after filtration of insoluble particles. Total and labile metal concentrations were determined by inductively coupled plasma mass spectrometry (ICP-MS, Agilent 7700, Agilent, Japan). Total and labile metal concentrations in total suspended particulate (TSP) were calculated by summation

140 of target metal concentrations in stages 1 to 6. Fractional Fe and Al solubility ($Fe_{sol}\%$ and $Al_{sol}\%$, respectively) and enrichment factors (EF) were calculated using the following equations:

$$Fe_{sol}\% = (labile\ Fe/total\ Fe) \times 100 \qquad (Eq.\ 1)$$

$$Al_{sol}\% = (labile\ Al/total\ Al) \times 100 \qquad (Eq.\ 2)$$

$$EF = (Fe/Al)_{aerosol}/(Fe/Al)_{crust}. \qquad (Eq.\ 3)$$

145 Iron and Al concentrations in the average continental crust were cited from Taylor (1964).

2.3. Major ion and water-soluble organic carbon concentrations

Major ions (Na^+, NH_4^+, K^+, Mg^{2+}, Ca^{2+}, Cl^-, NO_3^-, SO_4^{2-}, and $C_2O_4^{2-}$) in aerosol samples were extracted by the same methods for labile metal extractions. Water-soluble organic carbon (WSOC) was extracted using 15 mL of MQ water in glass

150 vials on a shaker for 1 hour. Major ions and WSOC concentrations were measured using ion chromatography (ICS-1100, Dionex, Japan) and a total carbon analyzer (TOC-V CSH, Shimadzu, Japan), respectively. Detail methods for ion chromatography are described in Sakata et al. (2014). Non-sea-salt (nss) SO_4^{2-} and Ca^{2+} were calculated by a following equation:

$$[nss\text{-}SO_4^{2-}\ or\ nss\text{-}Ca^{2+}] = [SO_4^{2-}\ or\ Ca^{2+}]_{aerosol} - [Na^+]_{aerosol} \times ([SO_4^{2-}\ or\ Ca^{2+}]/[Na^+])_{seawater} \qquad (Eq.\ 4)$$

155 To evaluate acidification degrees of mineral dust in aerosol particles, available proton for mineral dust ($[H^+]_{mineral}$) were evaluated (see Supplemental Methods). The $[H^+]_{mineral}$ is equal to the sum of $[NO_3^-]$ and $[nss\text{-}SO_4^{2-}]$ that are not associated with ammonium salt and aged sea spray aerosol. If $[H^+]_{mineral}$ is higher than [nss-Ca] ($[H^+]_{mineral} > 0$), mineral dust may have been acidified beyond the buffering capacity of $CaCO_3$.

2.4. Iron speciation by XAFS

160 Average Fe species in aerosol samples were determined using bulk XAFS spectroscopy at BL-9A and BL-12C in Photon Factory (PF), Ibaraki, Japan (Nomura and Koyama, 2001). Synchrotron radiation generated by bending magnet was monochromatized by a double-crystal monochromator of Si(111). The energy calibration was performed with the peak top of pre-edge peaks of hematite aligned to 7112 eV. Approximately 1/10 of collected aerosol samples on PTFE filters were

165 transferred to double-face carbon tape that oriented at 45° to the orthogonal direction of the incident X-ray beam. Iron K-edge XANES spectra of all target samples were recorded by fluorescence yield (FY) mode. The EXAFS spectra were simultaneously recorded with XANES for samples with Fe concentrations high enough to obtain EXAFS spectra. Scanning energies of XANES and EXAFS were 7080–7200 and 7080–7530 eV, respectively. All XANES and EXAFS spectra were recorded by

Atmospheric
Chemistry
and Physics
Discussions

fluorescence yield (FY) mode. Fluorescence X-ray from the samples was detected by a 19-element Ge solid-state detector

170   equipped with a Soller slit. Spectrum analysis of XANES and EXAFS spectra were performed by REX2000 Software (Rigaku, Japan). Energy region for LCF of XANES and EXAFS spectra was 7100–7200 eV and 0–10 Å in k-space, respectively.

Reference materials for inorganic Fe are ferrihydrite, goethite, hematite, biotite, chlorite, illite, smectite, montmorillonite, and Fe(III)-sulfate. Details of these references are described in Takahashi et al. (2011). Iron(II)-oxalate, Fe(III)-oxalate, Fe(III)-stearate, Fe(III)-nitrate, Fe(III) complexed with deferoxamine (Fe(III)-DFO) and Fe(III)-humate were employed as reference

175   materials of Fe(III)-organic complexes. Among them, Fe(III)-citrate, Fe(III)-stearate, Fe(III)-humate, and Fe(III)-DFO were defined as Fe(III)-HULIS in a broad sense. The Fe(III)-HULIS can be distinguished by Fe(III)-oxalate based on Fe K-edge XANES. The Fe K-edge XANES spectrum of Fe(III)-oxalate has two shoulders between 7120–7130 eV, whereas those of Fe(III)-HULIS has flatten peaks in the same region. To make it easier to compare XANES spectra between reference sand aerosol samples, the XANES spectrum of the reference materials sample is shown in Fig. 6b.

180

2.5. Al and Na speciation by XANES spectroscopy

Aluminium and Na speciation experiments were performed at BL-19B in PF and BL27SU in SPring-8, respectively. For both beamlines, synchrotron radiation generated by an undulator was monochromatized by the valid-line spacing plane grating monochromator (VLS-PGM). Aerosol samples on the carbon tape were installed in a vacuum chamber because of the short

185   attenuation length of soft X-ray (< 2000 eV) in the ambient atmosphere. The Al K-edge (1550–1600 eV) and Na K-edge (1065–1100 eV) XANES spectra of aerosol samples were recorded by FY mode. Fluorescence X-ray was detected by a single-element silicon drift detector.

2.6. Single-particle analysis

190   Single-particle analyses were conducted using scanning transmission X-ray microscopy (STXM) at BL-13A in PF (Takeichi et al. 2016). Monochromatic X-rays were focused to 30 nm × 30 nm by a Fresnel Zone Plate. The aerosol sample on the Mo grid was mounted on a piezo-controlled stage in a chamber purged with 0.1 atm He. Firstly, aerosol particles were imaged around energies in following: 280 eV (pre-edge), 285.0 eV (aromatic C), 287.6 eV (aliphatic C), 288.8 eV (carboxylic/hydroxamate C), carbonate (290.3 eV), and 297.2 eV (K L-edge), and 305 eV (post-edge). Iron, Na, and Al

195   distributions were identified image subtraction of post-edge from pre-edge. The typical imaging size was $15 \times 15 \ \mu m^2$ with $0.06 \times 0.06 \ \mu m^2$. After that, XANES spectra of C, K, Fe, Na, and Al were separately obtained by image stack mode. The typical imaging size for the image stack was $3 \times 3 \ \mu m^2$. Image drift was aligned after appending image stack data of all elements. The XANES spectra of the regions of interest (e.g., core and surface of the aerosol particles) were extracted using aXis2000 software.

200

2.7. Estimation of pH for proton-promoted dissolution (pH$_{PPD}$)

Average pH of proton-promoted dissolution (pH$_{PPD}$) was estimated using three Fe-pool model. The model was constructed based on a previous study on dissolution experiments using Beijing dust (Shi et al., 2011). Three Fe pools (fast, intermediate, and slow) have different dissolution rate constants according to the first-order kinetics (Shi et al., 2011). Observed

205 L-Fe concentration of aerosol particles ([L-Fe(t)]$_{aerosol}$) was described by the following equation:

$$[\text{L-Fe}(t)]_{aerosol} \ (ng/m^3) = [\text{L-Fe}(t)]_{fast} + [\text{L-Fe}(t)]_{intermediate} + [\text{L-Fe}(t)]_{slow} \qquad \text{(Eq. 6)}$$

$$[\text{L-Fe}(t)]_{fast/intermediate/slow} \ (ng/m^3) = [\text{obs-Fe}] \times [\%\text{Fe}(0)]_{fast/intermediate/slow} \times (1 - e^{-kt}) \qquad \text{(Eq. 7)}$$

where t is the dissolution time (h), [L-Fe(t)]$_{fast/intermediate/slow}$ is the labile Fe concentration (ng/m^3) at time t, [obs-Fe] is observed total Fe concentration, [%Fe(0)]$_{fast/intermediate/slow}$ is the percentage of solubilized Fe in each pool to total Fe, and k is dissolution

210 rate constant for each pool. Mineral dust is expected to undergo several condensation-evaporation cycles (one cycle: 12 hours) during transport, and the proton-promoted Fe dissolution occurs during the evaporation state (wet aerosol). Therefore, t is half of the transportation time estimated by backward trajectories. The %Fe(0) and k in each pool are basically pH-dependent (Table 1). Previous studies assumed illite as the major Fe species of Fe-containing mineral in the slow pool. However, weathered biotite was the dominant Fe-containing mineral in our samples (see Section 3.2.). Since the dissolution rate of biotite

215 is about an order of magnitude higher than those of illite (Bibi et al., 2011; Bray et al., 2015), the equation given in the previous study was rewritten as follows:

$$\text{Previous study: } \log k_{slow} = -0.44\text{pH} - 1.76. \qquad \text{(Eq. 8)}$$

$$\text{This study: } \log k'_{slow} = -0.44\text{pH} - 0.76. \qquad \text{(Eq. 9)}$$

Finally, pH (optional) was given to these equations to find the pH at which the observed L-Fe could be accounted within the

220 assumed transport time.

2.8. Geochemical modelling of L-Fe species

Aerosol liquid water (ALW) contents were calculated by E-AIM model IV (Clegg et al., 1992; Friese and Ebel, 2010), which can have an agreement of ALW between observational and modelled water mass has been reported by a previous study

225 (Engelhart et al., 2011). The input parameters for E-AIM Model IV were molar concentrations of H^+, Na^+, NH_4^+, Cl^-, NO_3^-, and SO_4^{2-}; temperature; and relative humidity. The proton concentration was estimated using the following equation:

$$[H^+] = [Cl^-] + [NO_3^-] + 2 \times [SO_4^{2-}] - [Na^+] - [NH_4^+] \qquad \text{(Eq. 10)}$$

The L-Fe species in aerosol liquid water (ALW) were calculated using the React model in GWB software (Bethke, 1996). Input data were molar concentrations of all major ions, oxalate ions, and labile metals (Al, Mn, Fe, Ni, Cu, Zn, Cd, Ba, and

230 Pb), WSOC, ALW, and temperature. The precipitations of metal species with high saturation index (> 1.0) were inhibited for simulation of the high ionic strength conditions of ALW (> few mol/L, Herrmann et al., 2015). The molar concentrations of WSOC were evaluated with three types of organic species: citric acid (C6), marine aliphatic carbon (C18, Cochran et al., 2016), and deferoxamine (C25). Furthermore, L-Fe species were calculated under various mixing ratio of WSOC to evaluate effects of internal mixing state between L-Fe and WSOC on L-Fe species. The mixing ratio is 1.0%, 2.5%, 5.0%, 10%, 25%, 50%

235 and 100% of WSOC concentration. For all calculations, the thermodynamic data of citric acid with Fe were used as a

representative organic ligand because the stability constant and acid dissociation constant of citric acid (log K: 13.13 and pKa_1: 3.13) are similar to those of HULIS (log K_{HULIS}: 11.1–13.9 and pK_a: 3.3–4.0, Salma and Láng, 2008; Samburova et al., 2008; Abualhaija et al., 2015). The initial pH was fixed at 7 and subsequently shifted from 7 to 0 to calculate the pH dependence of L-Fe species in the ALW. Total of 276 aqueous species were considered in the calculation, of which stability constants of the

240   main species are shown in Appendix in Supplemental Information.

3.   Results and Discussion

3.1. Total and labile Fe and Al concentrations in TSP

Backward trajectories analysis was performed by the Hybrid Single-Particle Lagrangian Integrated Trajectory model

245   (HYSPLIT, Stein et al., 2015). The WPO samples were affected by Asian continental outflows, whereas the air masses in CPO and WPO were derived from pelagic regions (Fig. 2). Total Fe and Al concentrations in TSP at the WPO samples (Figs. 3a and 3e, Fe: 75.6–257 ng/m^3, Al: 130–422 ng/m^3) were one to two orders of magnitude higher than those in the CPO and SPO (Figs. 3a and 3e, Fe: 0.733–4.37 ng/m^3, Al: 3.56–4.12 ng/m^3). Labile Fe and Al concentrations were also higher in WPO samples (Figs. 3b and 3f, Fe: 2.61–19.8 ng/m^3, Al: 3.56–27.0 ng/m^3) than CPO and SPO (Figs. 3b and 3f, Fe: 0.0422–0.0489

250   ng/m^3, Al: 0.0383–0.0678 ng/m^3). Thus, high total and labile metal concentrations were attributed to continental air masses (Figs. 2 and 3). Enrichment factors of Fe in these samples were 0.26–1.8 (0.92±0.55), indicating that Fe in these TSP samples were mainly derived from mineral dust (Fig. 3d). The Fe_{sol}% and Al_{sol}% in TSP were 5.30±2.99 % (0.967–7.69 %) and 3.32±2.22 % (1.08–6.40 %), respectively (Figs. 3c and 3g). These values were within a range reported by previous studies (Box 2 in Mahowald et al., 2018).

255

3.2. Size distributions of Fe and Al concentrations

The total Fe and Al concentrations in $PM_{1.3–10.2}$ were higher than those in $PM_{1.3}$ (Figs. 4a and 4d). Iron and Al in $PM_{1.3-10.2}$ were accounted for 78.5±8.34 % (n= 5, 69.9–87.9 %) and 81.8±8.53 % (n= 5, 72.0–88.8 %) in those of TSP, respectively. The enrichment factors of Fe and Ti as typical crustal elements were almost 1.0 regardless of aerosols diameter (Fig. S1). This

260   is because mineral dust is mainly present in $PM_{1.3-10.2}$. The labile concentrations of Fe and Al were higher in $PM_{1.3}$ than in $PM_{1.3–10.2}$ (Figs. 4b and 4e). Labile Fe and Al in $PM_{1.3-10.2}$ were accounted for 60.5±34.1 % (n= 5, 10.7–87.3 %) and 45.9±24.1 % (n= 5, 24.2–76.2 %) in those of TSP, respectively. Thus, size distributions of L-Fe and L-Al concentrations were clearly different from those of total Fe and Al. The average Fe_{sol}% in $PM_{1.3-10.2}$ and $PM_{1.3}$ were 2.56±2.53 % (n=20, 0.00–8.50%) and 22.3±21.7 % (n=10, 0.202–64.7 %), respectively (Fig. 4c). In the case of Al, the average Al_{sol}% in $PM_{1.3-10.2}$ and

265    $PM_{1.3}$ were 2.76±2.85 % (n=20, 0.389–11.5 %) and 11.7±10.8 % (n=10, 0.700–32.4 %), respectively (Fig. 4e). Thus, both Fe and Al in $PM_{1.3}$ were more soluble than those in $PM_{1.3-10.2}$. Therefore, even if the total Fe concentration in $PM_{1.3}$ was lower than $PM_{1.3-10.2}$, the $PM_{1.3}$ plays a significant role in supplying Fe in the ocean surface.

The enrichments of labile Fe and Al in fine fractions have been reported by previous studies (Baker and Jickells, 2006; Buck et al., 2010; Chance et al., 2015; Baker et al., 2020; Kurisu et al., 2021). One of the reasons for the enrichment of labile

270 Fe in fine fractions is the presence of pyrogenic Fe in fine fractions (Kurisu et al., 2021). Oil combustions, including ship emissions, are one of the dominant sources of pyrogenic Fe in fine aerosol particles because several studies have been reported associations of high Fe_{sol}% with high EF of V and Ni (Sedwick et al., 2007; Sholkovitz et al., 2009). However, Fe_{sol}% in $PM_{1.3}$ were not correlated with EF of V and Ni (Table S3, Spearman's correlation factor rho (ρ): 0.36 and -0.25 for V and Ni, respectively), which was consistent with a previous study (Buck et al., 2013). In contrast, Fe_{sol}% in $PM_{1.3}$ were correlated with

275 EF of Pb (Table S3, ρ: 0.75 for Pb), which were useful tracers for municipal solid waste incineration (MSWI) and coal combustions (Nriagu and Pacyna, 1988; Sakata et al., 2000, 2014). However, L-Fe in our samples were unlikely derived from anthropogenic sources because EFs of Fe in $PM_{1.3}$ were almost 1.0 above mentioned (Fig. S1). The $PM_{1.3}$ with high Fe_{sol}% (>10 %) contained available proton for mineral dust ($[H^+]_{mineral}$, see the Method section), whereas those in $PM_{1.3–10.3}$ and $PM_{1.3}$ with low Fe_{sol}% (<10 %) were near 0 or negative (Fig. 5a). Furthermore, the $[H^+]_{mineral}$ in $PM_{1.3}$ with high Fe_{sol}% was higher

280 than $[nss\text{-}Ca^{2+}]$, indicating that $[H^+]_{mineral}$ acidified mineral dust beyond the buffer capacity of $CaCO_3$ (Figs. 5b and 5c). In fact, Fe_{sol}% in $PM_{1.3}$ were also correlated with $nss\text{-}SO_4^{2-}$ (Table S3, ρ: 0.81), but a good correlation between Fe_{sol}% and oxalate was not observed (Table S3, ρ: 0.20). Therefore, it seems that aerosol acidification is more significant compared to organic complexations and anthropogenic emissions to solubilize Fe in $PM_{1.3}$.

In the case of WPO samples, it is considered that mineral dust was acidified during transportation in East Asia because

285 East Asia is a highly polluted area in the world. Previous studies showed that mineral dust in East Asian aerosol contained sulfate and oxalate as a proof of particle acidifications (Sullivan et al., 2007; Fitzgerald et al., 2015; Li et al., 2017; Sakata et al., 2021). Although $PM_{1.3}$ in the CPO sample did not pass over the highly polluted region, the S6-CPO has positive $[H^+]_{mineral}$ and high Fe_{sol}%. This result is probably due to the acidifications of mineral dust by SO_2 and H_2SO_4 derived from biogenic S (e.g., dimethylsulfide) because NH_3 gas cannot fully neutralized biogenic SO_2 and H_2SO_4 (Paulot et al., 2015; Nault et al.,

290 2021). In fact, the $nss\text{-}SO_4^{2-}$ concentration in S6-CPO was approximately an order of magnitude higher than that of NH_4^+ (Figs. S2a and S2b). Thus, Fe_{sol}% in $PM_{1.3}$ was enhanced by aerosol acidifications in not only polluted regions but also marine atmosphere.

3.3. Size dependence of Fe species in marine aerosols

295 Iron species in $PM_{1.3–10.2}$ were composed of two or three Fe species of hematite, ferrihydrite, biotite, and illite (Figs. 6a, 6c, and S3). More than half of the Fe in $PM_{1.3–10.2}$ was composed of biotite (Fig. 6a). The EXAFS spectra of $PM_{1.3-10.2}$ well reflected spectrum feature of biotite in 7–9 Å of k-space (Fig. S4), indicating that biotite was the dominant Fe species in $PM_{1.3-10.2}$. The relative abundance of ferrihydrite increased with decreasing aerosol diameter and with increasing transportation distances (Fig. 6a, WPO1 < WPO2 < WPO3 < SPO $\cong$ CPO). The hydration reaction of phyllosilicates in $PM_{1.3-10.2}$ forms

300 secondary ferrihydrite during transportations (Takahashi et al., 2011). Therefore, Fe in biotite in the $PM_{1.3-10.2}$ was partially altered to ferrihydrite. The Fe species in $PM_{1.3}$ with negative $[H^+]_{mineral}$ (S5-WPO1 and S6-SPO) were composed of the same

species in $PM_{1.3-10.2}$. The negative $[H^+]_{mineral}$ means that mineral dust was not acidified beyond the buffering capacities of $CaCO_3$. Therefore, Fe species in $PM_{1.3-10.2}$ and $PM_{1.3}$ were not drastically modified by aerosol acidification.

305 Iron(III)-HULIS and Fe(III)-sulfate were found as characteristic Fe species in $PM_{1.3}$ with $[H^+]_{mineral}$ and high Fe_{sol}% (>10%, Figs. 6a, 6c, and S3). Iron(III)-HULIS was present in all $PM_{1.3}$ with positive $[H^+]_{mineral}$, whereas only S6-WPO3 contained Fe(III)-sulfate with Fe(III)-HULIS (Fig. 6a). Since the source of Fe in $PM_{1.3}$ was mineral dust (Fig. S1), the Fe species at the time of emission was thought to be similar to that of coarse particles. However, the EXAFS spectra of $PM_{1.3}$ reflected spectrum features of Fe(III)-HULIS and Fe(III)-sulfate rather than biotite (Fig. S4). It seems that Fe(III)-sulfate and Fe(III)-HULIS were formed by secondary processes of biotite during transport. It is known that oxalate is one of the important ligands to enhance Fe_{sol}% in aerosol particles (Chen and Grassian, 2013; Ito and Shi, 2016; Hamilton et al., 2019), the presence or the absence of Fe(III)-oxalate in these samples were examined. As a result, the abundance of the Fe(III)-oxalate in these samples was not dominant Fe species in our samples by the LCF. This result is consistent with the fact that there is no correlations between Fe_{sol}% and oxalate concentrations (Table S3).

315 For comparison, Fe species in East Asian aerosols (Beijing and NOTOGRO) were determined by XAFS spectroscopy. Beijing dust also contained Fe(II)-sulfate and Fe(III)-sulfate with ferrihydrite and biotite (Fig. S5). Iron species in $PM_{1.3-10.2}$ collected in the NOTGORO were composed of illite, smectite, biotite and ferrihydrite, which species were similar to those in $PM_{1.3-10.2}$ in marine aerosol particles (Figs. 6a and 6d), whereas Fe(II)-sulfate and Fe(III)-oxalate was found in $PM_{1.3}$ collected in the NOTOGRO (Figs. 6a and 6c). The EXAFS spectrum of the S6-NT has single peak in 7–9 Å of k-space, whereas those of $PM_{1.3-10.2}$ has two peaks of biotite in the same regions (Fig. S4e). Therefore, Fe(II)-sulfate and Fe(III)-oxalate were formed by chemical alteration of biotite, which was consistent with Fe speciation results of WPO. Iron(III)-HULIS was not assigned as the dominant Fe species in NOTOGRO and Beijing dust (Figs. 6a, 6c and S5). These results indicated that Fe(III)-HULIS in the WPO samples was possibly formed by chemical alteration of Fe(II, III)-sulfates and Fe(III)-oxalate after aerosol pass over Japan.

To identify L-Fe species in $PM_{1.3}$, Fe K-edge XANES spectra of insoluble Fe in the S6-WPO2 were recorded after water 325 extractions of labile Fe species. As a result, the XANES spectra of total Fe (= labile + insoluble Fe) was well fitted by insoluble Fe and Fe(III)-HULIS (Fig. S3d). Furthermore, the Fe_{sol}% in $PM_{1.3}$ were correlated with the abundance of Fe(III)-HULIS (Fig. 6e). Therefore, Fe(III)-HULIS is an important L-Fe species in $PM_{1.3}$ in the marine atmosphere.

3.4. Size dependence of Al species

330 Given that Fe(III)-HULIS was formed by chemical alterations of Fe in biotite, Al species in $PM_{1.3}$ may be different from those in $PM_{1.3-10.2}$. Therefore, we determined Al species in WPO2 and WPO3 using XANES spectroscopy. The Al species in $PM_{1.3-10.2}$ were composed of octahedral Al and tetrahedral Al, of which Al K-edge XANES spectra were similar to those of biotite (Fig. 7). The Al K-edge XANES spectra of $PM_{1.3-10.2}$ were well fitted by each other. This result implies that (i) the sources of Al emissions were similar among $PM_{1.3-10.2}$, and (ii) Al species in these samples were not changed significantly 335 during transport. In contrast, secondary Al species were identified in $PM_{1.3}$. The S5-WPO2 and S5-WPO3 contained gibbsite

Atmospheric
Chemistry
and Physics
Discussions

Open Access

EGU

and phyllosilicates (Fig. 7). The S6-WPO3 contained Al-sulfate and organic complexes of Al (organo-Al) in addition to phyllosilicates in $PM_{1.3}$ and gibbsite, which was consistent with the presence of Fe(III)-sulfate in this sample (Figs 6a and 8). In the case of S6-WPO2 with the highest abundance of Fe(III)-HULIS, the Al K-edge XANES spectrum was totally different from that of phyllosilicates in $PM_{1.3-10.2}$, though the XANES spectrum of S6-WPO2 could not be fitted by the reference

340   materials examined in this study. Given that initial Al species in $PM_{1.3}$ were phyllosilicate as was for $PM_{1.3-10.2}$, it is possible that phyllosilicate particles were altered in the atmosphere. This result is consistent with the absence of the spectrum feature of biotite in Fe K-edge EXAFS spectra of $PM_{1.3}$.

3.5. Single particle analysis

345   Single-particle analysis in S6-WPO2 was conducted using STXM to evaluate the alteration processes of Fe-bearing phyllosilicate particles. Iron-bearing particles have irregular shapes (Figs. 8 and S6–S8). This morphological feature was similar to naturally occurring phyllosilicate particles (Matsuki et al., 2005; Jeong and Nousiainen, 2014). In contrast, anthropogenic Fe (e.g., fly ash and pyrogenic hematite) has spherical shapes which were not dominated in S6-WPO2 (Li and Shao, 2009; Adachi et al., 2021). Therefore, Fe-bearing particles with irregular shapes and high OD_{C-pre} were phyllosilicate

350   particles. These Fe-bearing phyllosilicates were covered with Na and OCs. Organic carbons on mineral dust were mainly presented as aliphatic species because the peaks of aliphatic C and carboxylates were dominated in the C K-edge NEXAFS spectra (Fig. 8 and S8). The C K-edge NEXAFS spectra of OCs on the mineral surface were similar to those in submicron sea spray aerosol SSA (Prather et al., 2013; Wilson et al., 2015). Furthermore, the Na K-edge XANES spectra on the particle surface were also similar to Na salt with organic acids rather than inorganic Na (Fig. S9). It is known that submicron sea spray

355   aerosol (SSA) and marine cloud water contained both Na and OCs (Mochida et al., 2002; Straub et al., 2007; Cochran et al., 2016; Bikkina et al., 2019). In fact, the Na speciation result also showed that $PM_{1.3}$ collected in WPO2 and WPO3 contained organic Na salts, whereas Na species in $PM_{1.3-10.2}$ was composed of only NaCl (Fig. S9). Therefore, submicron SSA or marine cloud water is one of the sources of Na and OCs on the phyllosilicate surface. The surface coating of Na and OCs contributed to chemical alteration of phyllosilicate particles because Al K-edge XANES spectra of these particles were similar to that in

360   humic substances (SRFA, Fig. 7). Thus, phyllosilicate particles in $PM_{1.3}$ were intensely altered during transport from East Asia to the WPO.

4.   Discussion

4.1. Reconstruction alteration processes of Fe based on pH_{PPD} and pH_{L-Fe}

365   Our observation results showed that L-Fe in aerosol particles were mainly controlled by Fe in $PM_{1.3}$ (Fig. 4b). Aerosol acidification was one of the factors of enhancement of L-Fe concentrations because (i) $PM_{1.3}$ with high Fesol% (>10%) has positive $[H^+]_{mineral}$ (Fig. 5a), and (ii) L-Fe concentration correlated with $[nss-SO_4^{2-}]$ (Table S3). Furthermore, the fraction of Fe(III)-HULIS correlated with $Fe_{sol}\%$ in aerosol particles (Fig. 6e). Therefore, it is likely that both aerosol acidification and organic complexation of Fe contributed to the enhancement of $Fe_{sol}\%$. Here, reaction pH for proton-promoted dissolution

370   (pH$_{PPD}$) and formation of L-Fe species (pH$_{L-Fe}$) were evaluated using conceptual and geochemical models, respectively. Firstly, the modelled L-Fe concentration in PM$_{1.3}$ with negative [H$^+$]$_{mineral}$ was much higher than the observed L-Fe concentration, even though pH$_{PPD}$ was set as 3.0 (Fig. S10). This result indicated that Fe-bearing particles in these samples were not acidified to pH 3.0. Consequently, Fe in these samples was not sufficiently solubilized by atmospheric processes. In fact, Fe species in these samples were similar to those in PM$_{1.3-10.2}$ with low Fe$_{sol}$%.

375   The observed L-Fe concentrations in PM$_{1.3}$ with positive [H$^+$]$_{mineral}$ were reproduced when pH was lower than 3.0 (Figs. 9 and S11). This result is consistent with previous studies because the high Fe$_{sol}$% was observed when aerosol pH was lower than 3.0 (Fang et al., 2017; Tao and Murphy, 2019). As previously mentioned, Fe in biotite was altered to Fe(III)-HULIS and/or Fe(III)-sulfate (Fig. S4). Previous studies showed that octahedral layer of phyllosilicate including biotite were preferentially decomposed under highly acidic conditions (pH < 3.0) and Fe in biotite is mainly present in the octahedral layer

380 (Shaw et al., 2009; Bray et al., 2015). Therefore, it is reasonable that Fe$_{sol}$% increases rapidly when the pH drops below 3.0. Modelled L-Fe species in PM$_{1.3}$ with positive [H$^+$]$_{mineral}$ were present as Fe(III)-sulfate or Fe(III)-oxalate under acidic conditions (pH$_{L-Fe}$ < 3.0) with any ratios of [citrate]/[oxalate] and [citrate]/[L-Fe], though stability constants of citrate is much higher than that of oxalate and sulfate (Fig. 9 and S12–16). This phenomenon can be ascribed to the fact that citric acid forms fully protonated species below its pK$_{a1}$ (= 3.13), whereas oxalate and sulfate can form ferric complexes even at pH < 3.0 (Fig.

385 9 and S12–16). As previously mentioned, East Asian aerosol particles contained Fe(II, III)-sulfate and Fe(III)-oxalate, but Fe(III)-HULIS was not dominant Fe species (Figs. 6a, 6d and S5). Therefore, it is considered that mineral dust in the WPO samples encountered the highly acidic conditions during transportation in East Asia.

     In contrast, the geochemical model showed that Fe(III)-HULIS was dominant under moderately acidic conditions (pH$_{L-Fe}$ 3.0–6.0), where [citrate]/[L-Fe] was higher than 1.0 (Figs. 10b and S12–S16). In the case of S6-WPO3, the coexistence of

390 Fe(III)-HULIS and Fe(III)-sulfate was found under only moderately acidic conditions, when [citrate]/[L-Fe] was between 0.30 and 0.45 (Figs. 9d and S16). Therefore, the pH of phyllosilicate should be increased after proton-promoted processes to form the Fe(III)-HULIS. Single-particle analyses identified the presence of surface coating of Na and OCs on phyllosilicate particles, which was caused by internal mixing with submicron SSA or marine cloud water. A recent mesocosm experiment showed that submicron SSA is rapidly acidified to pH 2.0 because of water evaporation, uptake of acidic gases and/or displacement reaction

395 of proton in organic acids by Na$^+$ (Angle et al., 2021). Our Na speciation results showed that organic salt of Na was present in submicron SSA (Fig. S8). If submicron SSA in ambient atmosphere has high aerosol acidity, the internal mixing of phyllosilicates and submicron SSA may not sufficiently increase the pH of phyllosilicates.

     Another candidate is the evaporation-condensation cycles (cloud process) during transportation. The marine cloud water also can form Na and OCs coating on the phyllosilicate particles because Na and OCs as dominant components in the marine

400 cloud water (Straub et al., 2007). Given that 500 nm of phyllosilicate particles with a 100 nm-thick water layer at pH 1.0 was incorporated into typical marine cloud water (diameter 10 μm, pH 4.0, Boris et al., 2016; Kim et al., 2019; Shah et al., 2020), the pH of the cloud water decreased by only 0.03 pH unit. The increase in aerosol pH by cloud processes decreases Fe$_{sol}$% because of the precipitation of nano-ferrihydrite with the sole consideration of inorganic Fe chemistry (Spokes et al., 1994;

Shi et al., 2015; Maters et al., 2016). However, the nano-ferrihydrite precipitations were suppressed by the formation of Fe(III)-
405 HULIS due to its high solubility. As a result, L-Fe obtained by proton-promoted dissolution below pH 2.0 was retained under
moderately acidic conditions. Therefore, the role of HULIS is not to promote further Fe dissolution from aerosol particles, but
to stabilize the L-Fe under moderately acidic conditions. This result was consistent with a previous laboratory experiment
(Paris and Desboeufs, 2013).

In summary, Fe in $PM_{1.3}$ was solubilized by the proton-promoted dissolution, and subsequently solubilized Fe were
410 stabilized as L-Fe by organic complexation with HULIS in the cloud processes (Fig. 10). In the case of WPO samples, aerosol
acidification and stabilization of L-Fe was caused in East Asia and the Pacific Ocean, respectively. This result is consistent
with the hypothesis suggested by Buck et al. (2013). The studies implied that atmospheric processing after passing over Japan
are not important to solubilize Fe because significant differences of $Fe_{sol}\%$ in the North Pacific Ocean has not been observed
(Buck et al., 2013). The stabilization of L-Fe species may play a critical role in the supply of dissolved Fe from aerosol
415 particles to the ocean surface. Given that log K_{HULIS} in aerosol particles is a strong ligand on the ocean surface (L_1, log
K >12), Fe(III)-HULIS dissolved without the consumption of L_1 ligands on the ocean surface. This phenomenon possibly
promoted further Fe dissolution with moderately water-soluble species (e.g., nano-ferrihydrite) by complexation with
the L_1 or weaker ligands (L_2, log K: 11–12) on the ocean surface (Gledhill and Buck, 2012). When log K_{HULIS} was similar
to weak or super-weak ligands (log K < 11), the probabilities of encountering L_1 and L_2 ligands with Fe(III)-HULIS
420 increased by the expanding lifetime of dissolved Fe (hours to days, Meskhidze et al., 2017). Thus, Fe(III)-HULIS
strongly influences the fate of dissolved Fe in the ocean from aerosol particles. Further investigations of atmospheric
organic ligands combined with Fe in aerosol particles are necessary to extend our knowledge on the biogeochemical
cycle of Fe.

425 **4.2. Importance of size-fractionated aerosol particles**

Thus, Fe in $PM_{1.3}$ was solubilized by atmospheric processes during transportation. These results could not be
obtained if we collected TSP rather than size-fractionated aerosol particles. This is because the abundance of Fe(III)-
HULIS is approximately 5% of total Fe in TSP, which was below the detection limit of XAFS spectroscopy. Previous
studies have also suggested the presence of Fe(III)-sulfate as L-Fe species by spot analysis using microscopic XAFS,
430 but Fe(III)-sulfate were not detected by macroscopic XAFS because of lower abundance of the species in TSP (Oakes et
al., 2012; Kurisu et al., 2021). Therefore, size-fractionated aerosol sampling is needed to identify L-Fe species in the
marine aerosol particles.

In general, the cutoff diameter for size-fractionated aerosol sampling is 2.5 μm, but this may not be enough to
separate the L-Fe species with high $Fe_{sol}\%$ from the less aged mineral dust. Our results showed that high $Fe_{sol}\%$

435   associated with Fe(III)-HULIS was found in $PM_{1.3}$. In contrast, aerosol particles in stage-4 (hereafter, $PM_{1.3-2.3}$ is described as $PM_{1.0-2.5}$ for the simplification) did not have high $Fe_{sol}\%$ because mineral dust in the fractions was not acidified beyond the buffering capacity of $CaCO_3$. This result is consistent with previous studies because aerosol pH in $PM_{1.0-2.5}$ was higher than those in $PM_{1.0}$ because of larger and smaller contributions of non-volatile cations (e.g., Ca and Na) and sulfates in $PM_{1.0-2.5}$ compared to $PM_{1.0}$, respectively (Fang et al., 2017; Guo et al., 2018). Furthermore, in the

440   case of our sample, about 40% (11.9-58.9%) of the total Fe in $PM_{2.5}$ was contained in $PM_{1.0-2.5}$. In the analysis of the $PM_{2.5}$, the relative abundances of L-Fe concentrations in $PM_{1.0}$ were diluted by insoluble Fe in $PM_{1.0-2.5}$. This is also true for the investigation of pyrogenic Fe with high $Fe_{sol}\%$. Previous studies showed that low Fe isotope ratio associated with pyrogenic Fe was found in $PM_{1.3}$, whereas the isotope ratio in $PM_{1.0-2.5}$ was similar to Fe in crustal materials (Kurisu et al., 2016, 2019). For these reasons, two-stage aerosol sampling with a cutoff diameter of 1.0 μm or multi-stage aerosol

445   sampling is desirable to investigate the factors controlling the $Fe_{sol}\%$ in marine aerosol particles. Since size-fractionated aerosol sampling recovered small amount of sample er each staged compared to TSP sampling (Sakata et al., 2018; Baker et al., 2020), the developments of analytical techniques for low concentration of trace metal are essential.

5.   Conclusions

450   In this study, size-fractionated aerosol particles were collected in the Pacific Ocean. About 80% of total Fe were present in $PM_{1.3-10.2}$, whereas $PM_{1.3}$ accounted for about 60% of L-Fe in TSP. The average $Fe_{sol}\%$ in $PM_{1.3}$ (22.3±21.7%) was about an order magnitude of higher than that in $PM_{1.3-10.2}$ (2.56±2.53%). The Fe species in $PM_{1.3-10.2}$ were ferrihydrite, hematite, biotite, and illite. These Fe were similar to those in mineral dust. The Fe in $PM_{1.3-10.2}$ was not well solubilized during transportation because mineral dust in the fraction was not acidified beyond the buffering capacity of $CaCO_3$. In the case of $PM_{1.3}$ with

455   positive $[H^+]_{minerals}$, Fe(III)-HULIS was present as specific L-Fe species in $PM_{1.3}$. The species were formed by the chemical alteration of biotite. The chemical alteration of biotite in $PM_{1.3}$ was confirmed by bulk Al speciation and single-particle analysis of mineral dust because secondary Al species (e.g., gibbsite, Al-sulfate, and organo-Al) were present in the $PM_{1.3}$. Thus, the Al species can be used as a good indicator of the degree of phyllosilicate alterations. As a result of pH estimation using a conceptual model, Fe in mineral dust was solubilized under highly acidic conditions (pH < 3.0). Subsequently, Fe(III)-HULIS

460   was formed in marine cloud water under moderately acidic conditions (3.0 < pH < 6.0). The role of the complexation reaction of Fe with HULIS is the stabilization of L-Fe rather than the further promotion of Fe dissolution from aerosol particles. At present, thermodynamic data of HULIS with Fe in $PM_{1.3}$ are not enough to evaluate the effects of HULIS on Fe dissolution. Therefore, further observations and laboratory experiments on the complex formation between HULIS and Fe are expected to improve our understanding of the effect of HULIS on Fe dissolution.

465

Atmospheric
Chemistry
and Physics
Discussions

Open Access

EGU

Supplement. The supplement related to this article is available online at XXXX.

485 **Figure captions**

Figure 1: Track chart of the research cruise of KH-14-6 (R/V Hakuho-Maru) and sampling locations of WPO, CPO and SPO samples. Red circle showed the locations of Beijing and Noto Ground-Based Research Observatory (NOTOGRO).

Figure 2: Backward trajectories of (a) WPO1, (b) WPO2, (c) WPO3, (d) CPO, and (e) SPO obtained by the ensemble mode. The backward trajectories were calculated at midpoint of each sampling region shown in Fig. S1. Duration of WPO1

490 to WPO3 were 5 days, where those for CPO and SPO samples were 7 days.

Figure 3: (a) total Fe (ng/m^3), (b) labile Fe (ng/m^3), (c) Fe_{sol}%, (d) EF of Fe, (e) total Al (ng/m^3), (f) labile Al (ng/m^3), and (g) Al_{sol}% in TSP.

Figure 4: Size distributions of (a) total Fe (ng/m^3), (b) labile Fe (ng/m3) (c) Fe_{sol}%, (d) total Al (ng/m3), (e) labile Al (ng/m3), and (f) Al_{sol}%. The $PM_{1.3}$ is shown in yellow regions.

495 Figure 5: (a) A scatter plot between Fe_{sol}% and $[H^+]_{mineral}$. The blue region shows positive $[H^+]_{mineral}$. Size distributions of (b) $[H^+]_{mineral}$l and (c) $nss-Ca^{2+}$. The $PM_{1.3}$ is shown in yellow regions.

Figure 6: (a) Fraction of Fe species in each sample determined by Fe K-edge XANES spectroscopy. (b) Fe K-edge XANES spectra of reference materials. Colored spectra were used as reference materials for LCF, whereas black spectra were not assigned as dominant Fe species in our samples. Iron K-edge XANES spectra of size-fractionated aerosol

500 particles collected in (c)WPO2 and (d) NOTOGRO. (d) a scatter plot between fraction of Fe(III)-HULIS and Fe_{sol}%.

Figure 7: Al K-edge XANES spectra of (a) WPO2 and (b) WPO3. Black and red solid line showed XANES spectra for aerosol particles and fitting spectra, respectively. Colored spectra with dashed line show fitting components. The Al K-edge XANES spectra of particle 1 to particle 3 in panel (a) were obtained by single particle analysis using STXM. The X-ray image of these particles are shown in Figure 9.

505 Figure 8: (a-1 and b-1) X-ray image at post-edge of C K-edge of single aerosol particles in S6-WPO2. (a-2 and b-2) RGB composites of Fe (R: red), carboxylates (G: green), and Na (B: blue). Distributions of carboxylates (OCs), K, Fe, Na, and Al are shown in panels (a-3 and b-3), (a-4 and b-4), (a-5 and b-5), (a-6 and b-6), and (a-7 and b-7), respectively. (a-8 and b-8) Carbon K-edge XANES spectra on the surface of each phyllosilicate particle. Particle 1 in panel (a) was covered with tiny amounts of OCs, whereas particles 2 and 3 in panel b is covered with aliphatic C. Gray, light green,

510 pink, light blue, orange, and brown regions show the peak positions of aromatic C, ketonic C, aliphatic C, carboxylates, carbonate, and potassium, respectively.
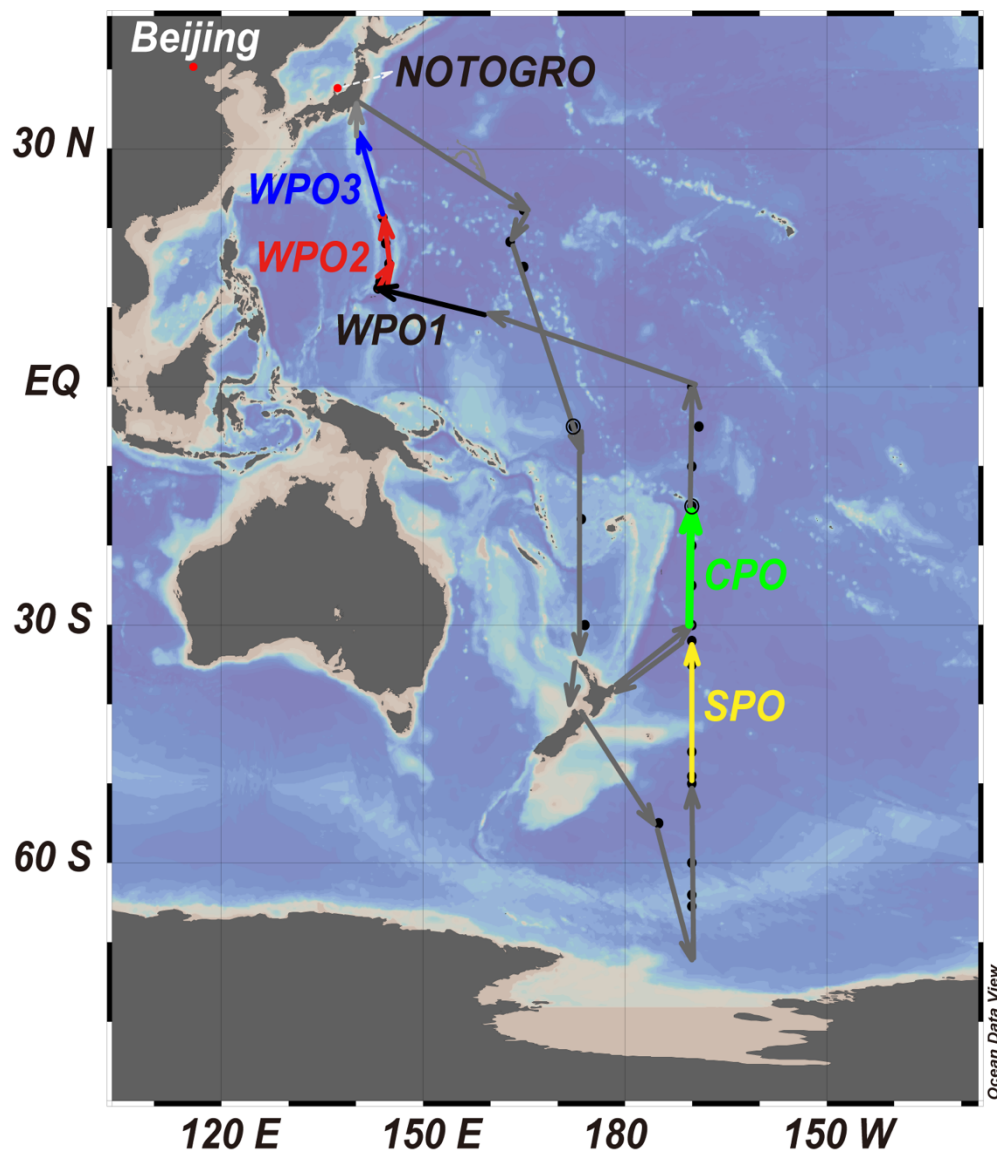
Figure 9: (a and c) dissolution curves for each Fe pool (colored dashed lines) and summation of all Fe pools (solid black line) in S6-WPO2 and S6-WPO3 as a function of dissolution time. Solid red line in these figures shows the observed L-Fe concentrations. The pH was set so that the total value reached the observed L-Fe in approximately 60 h (expected

515 time for wet aerosol phase). (b and d) pH dependences of L-Fe species in ALW for S6-WPO2 and S6-WPO3. Pink

Atmospheric
Chemistry
and Physics
Discussions
Open Access
EGU

and yellow regions show the aerosol pH for the proton-promoted dissolution (same pH as in panels a and c) and stable pH regions of Fe(III)-HULIS, respectively.

Figure 10: The schematic of alteration processes of Fe in phyllosilicate particles in $PM_{1.3}$ during transport.

520

525 Figure 1: Track chart of the research cruise of KH-14-6 (R/V Hakuho-Maru) and sampling locations of WPO, CPO and SPO samples. Red circle showed the locations of Beijing and Noto Ground-Based Research Observatory (NOTOGRO). The figure was described using Ocean Data View (Schlitzer, 2021).
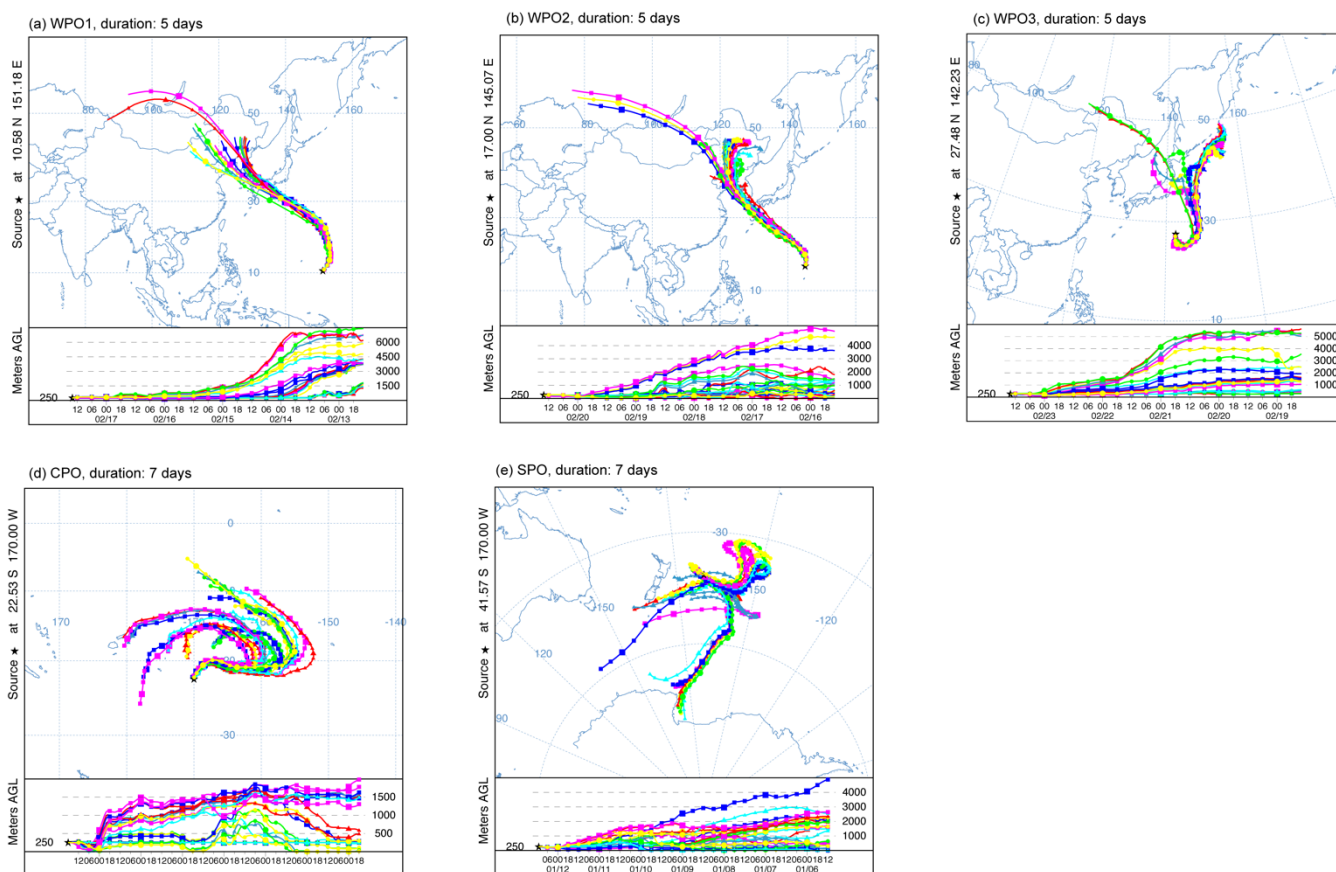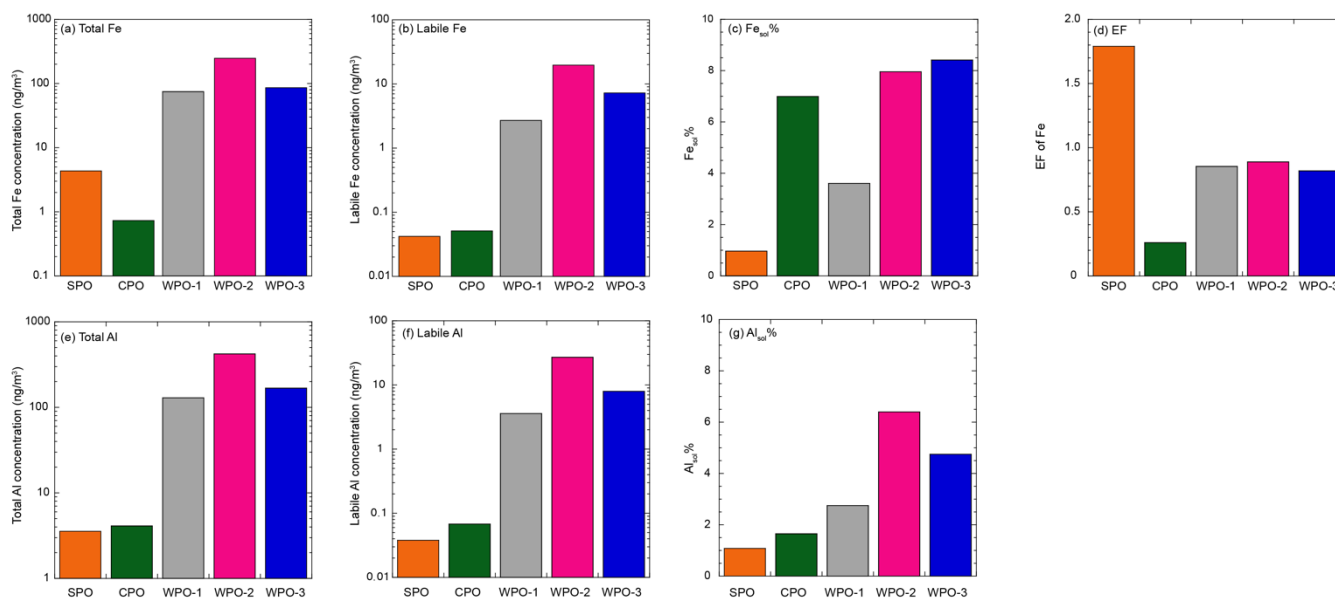
530

535

Figure 2: Backward trajectories of (a) WPO1, (b) WPO2, (c) WPO3, (d) CPO, and (e) SPO obtained by the ensemble mode. The backward trajectories were calculated at midpoint of each sampling region shown in Fig. S1. Duration of WPO1 to WPO3 were 5 days, where those for CPO and SPO samples were 7 days.

540

Atmospheric
Chemistry
and Physics
Discussions
Open Access
EGU

545

550 Figure 3: (a) total Fe (ng/m^3), (b) labile Fe (ng/m^3), (c) Fe$_{sol}$%, (d) EF of Fe, (e) total Al (ng/m^3), (f) labile Al (ng/m^3), and (g) Al$_{sol}$% in TSP.
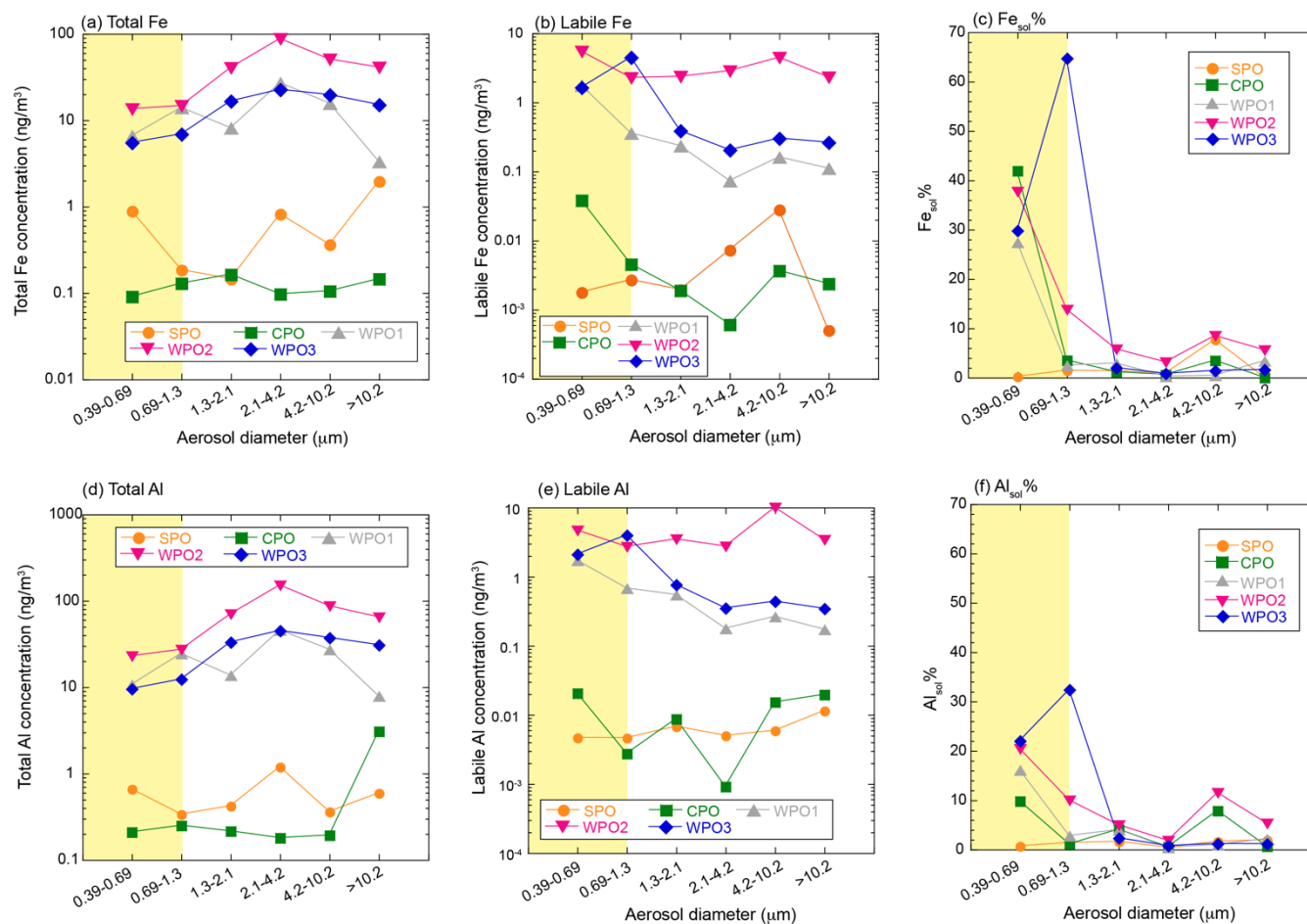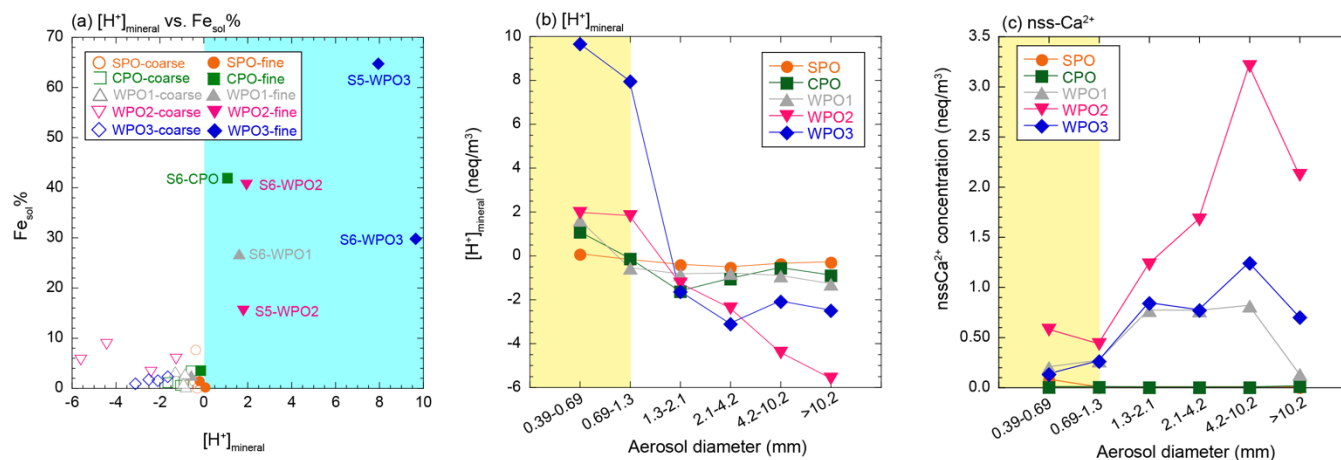
555

560

Figure 4: Size distributions of (a) total Fe (ng/m^3), (b) labile Fe (ng/m^3) (c) Fe$_{sol}$%, (d) total Al (ng/m^3), (e) labile Al (ng/m^3), and (f) Al$_{sol}$%. The PM$_{1.3}$ is shown in yellow regions.

565

570

575

Figure 5: (a) A scatter plot between $Fe_{sol}\%$ and $[H^+]_{mineral}$. The blue region shows positive $[H^+]_{mineral}$. Size distributions of (b) $[H^+]_{mineral}$ and (c) nss-Ca^{2+}. The $PM_{1.3}$ is shown in yellow regions.

Atmospheric
Chemistry
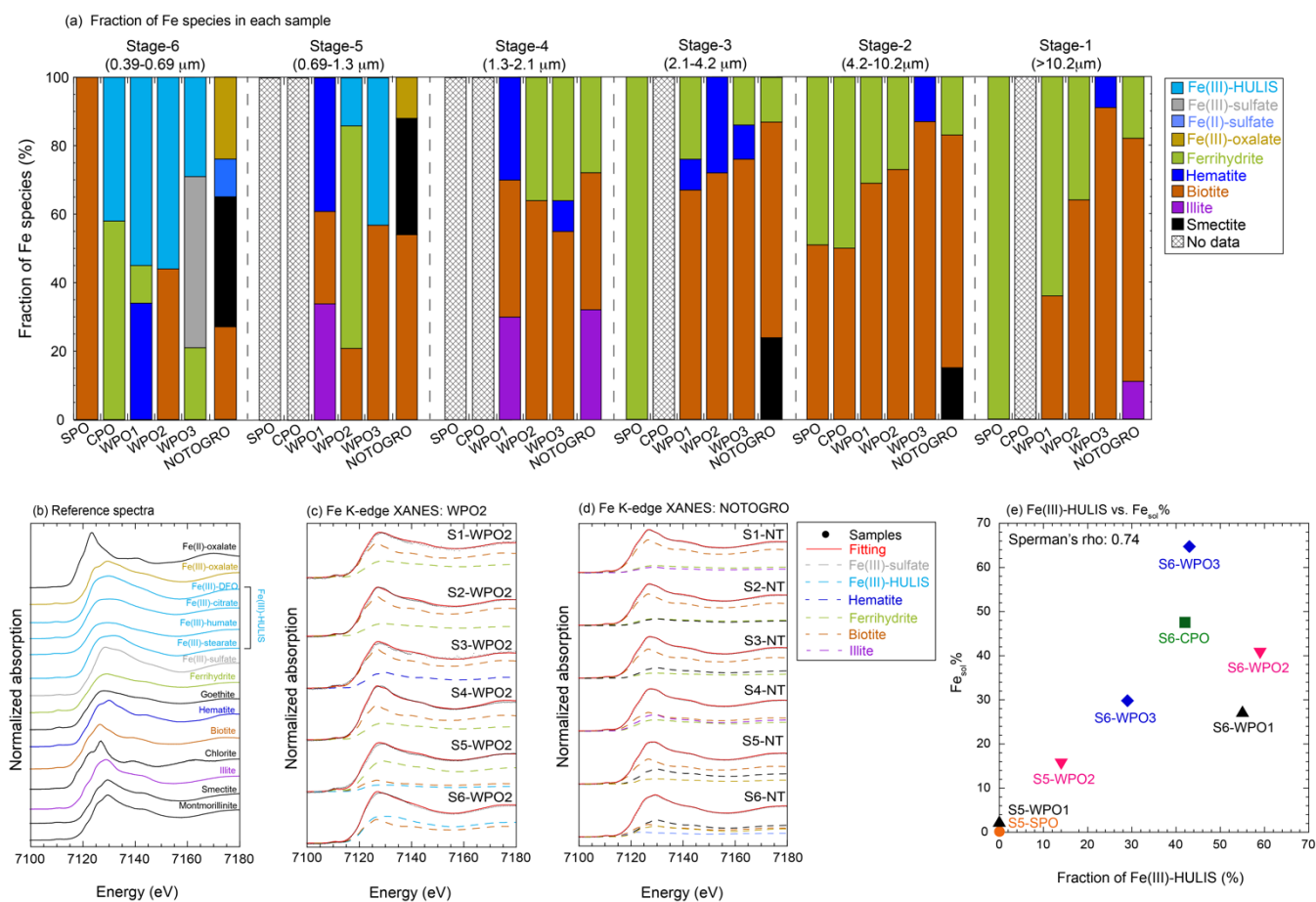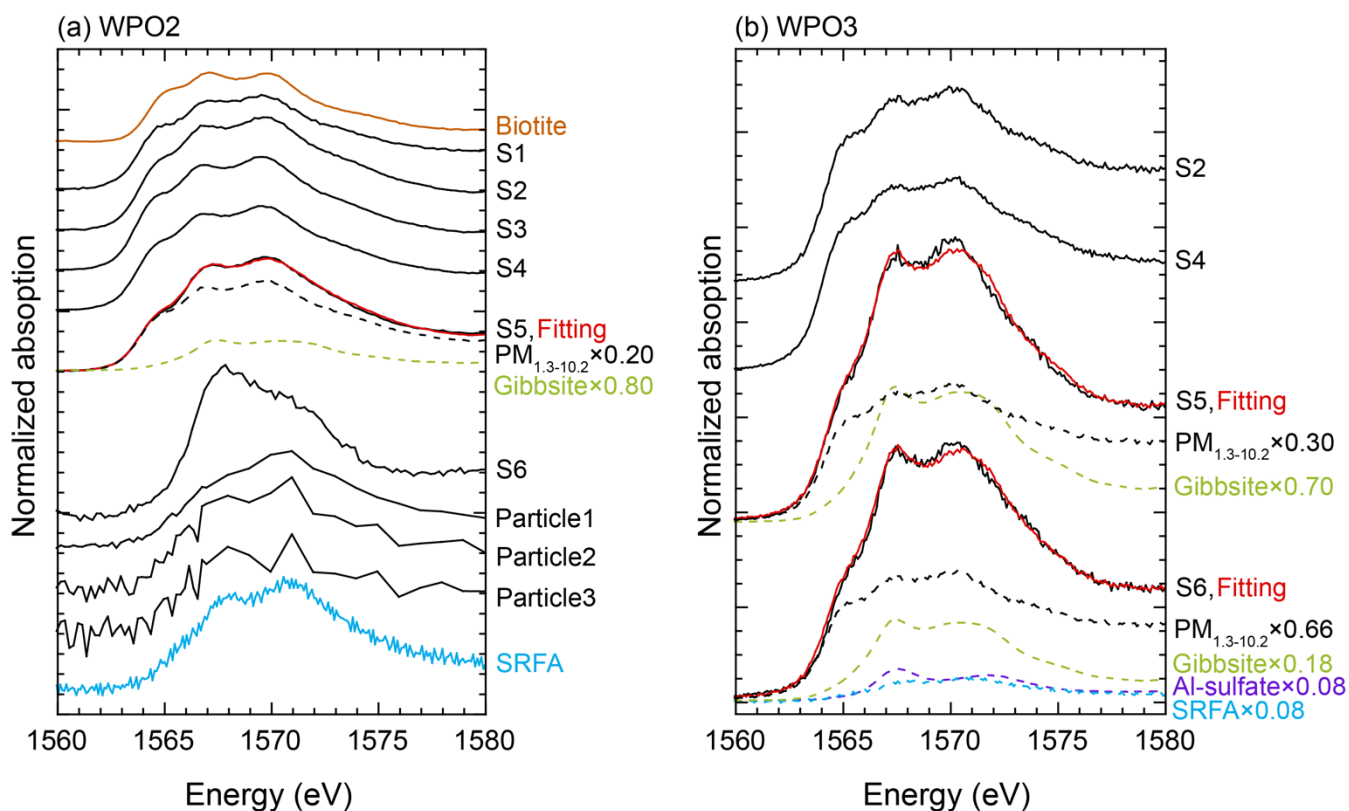and Physics
Discussions

Open Access

EGU

580

Figure 6: (a) Fraction of Fe species in each sample determined by Fe K-edge XANES spectroscopy. (b) Fe K-edge XANES
spectra of reference materials. Colored spectra were used as reference materials for LCF, whereas black spectra were
585   not assigned as dominant Fe species in our samples. (c) Fe K-edge XANES spectra of size-fractionated aerosol
particles collected in WPO2 and their fitting components. (d) a scatter plot between fraction of Fe(III)-HULIS and
$Fe_{sol}\%$.

590

Figure 7 Al K-edge XANES spectra of (a) WPO2 and (b) WPO3. Black and red solid line showed XANES spectra for aerosol particles and fitting spectra, respectively. Colored spectra with dashed line show fitting components. The Al K-edge XANES spectra of particle 1 to particle 3 in panel (a) were obtained by single particle analysis using STXM. The X-ray image of these particles are shown in Figure 9.

600
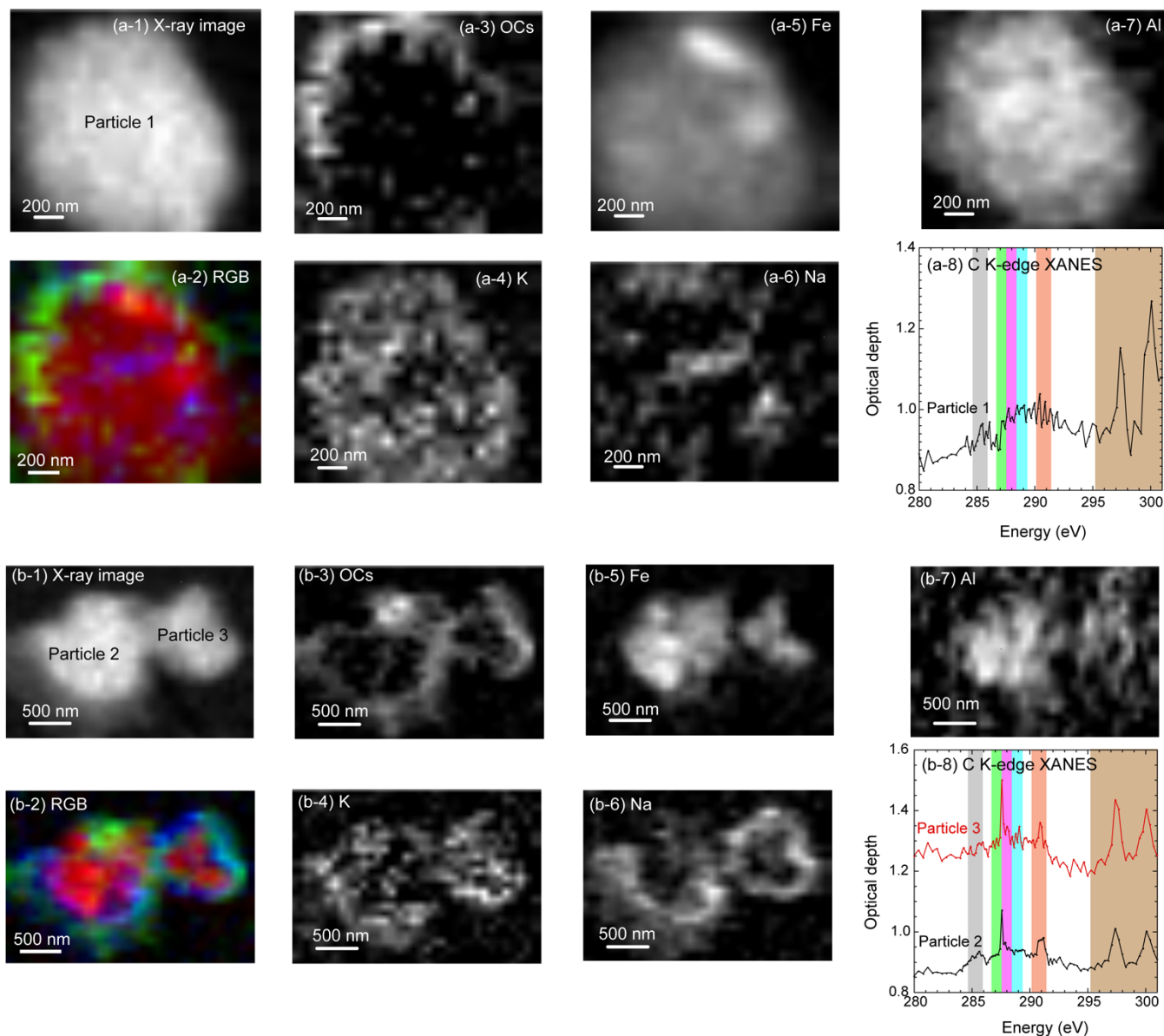
Figure 8 (a-1 and b-1) X-ray image at post-edge of C K-edge of single aerosol particles in S6-WPO2. (a-2 and b-2) RGB composites of Fe (R: red), carboxylates (G: green), and Na (B: blue). Distributions of carboxylates (OCs), K, Fe, Na, and Al are shown in panels (a-3 and b-3), (a-4 and b-4), (a-5 and b-5), (a-6 and b-6), and (a-7 and b-7), respectively. (a-8 and b-8) Carbon K-edge XANES spectra on the surface of each phyllosilicate particle. Particle 1 in panel (a) was covered with tiny amounts of OCs, whereas particles 2 and 3 in panel b is covered with aliphatic C. Gray, light green, pink, light blue, orange, and brown regions show the peak positions of aromatic C, ketonic C, aliphatic C, carboxylates, carbonate, and potassium, respectively.
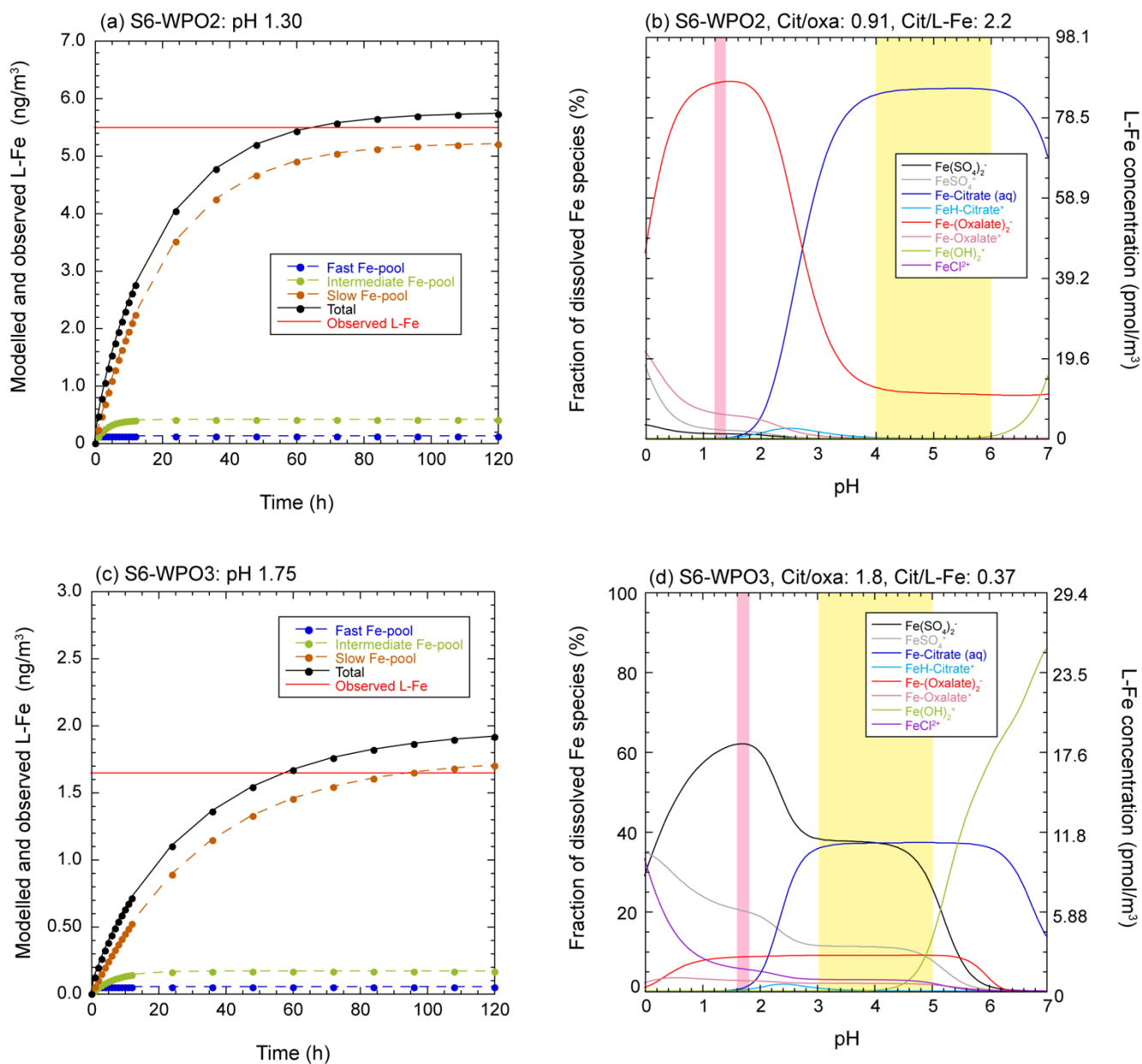
Figure 9: (a and c) dissolution curves for each Fe pool (colored dashed lines) and summation of all Fe pools (solid black line) in S6-WPO2 and S6-WPO3 as a function of dissolution time. Solid red line in these figures shows the observed L-Fe concentrations. The pH was set so that the total value reached the observed L-Fe in approximately 60 h (expected time for wet aerosol phase). (b and d) pH dependences of L-Fe species in ALW for S6-WPO2 and S6-WPO3. Pink and yellow regions show the aerosol pH for the proton-promoted dissolution (same pH as in panels a and c) and stable pH regions of Fe(III)-HULIS, respectively.

27

620

Figure 10: The schematic of alteration processes of Fe in phyllosilicate particles in $PM_{1.3}$ during transport.

625
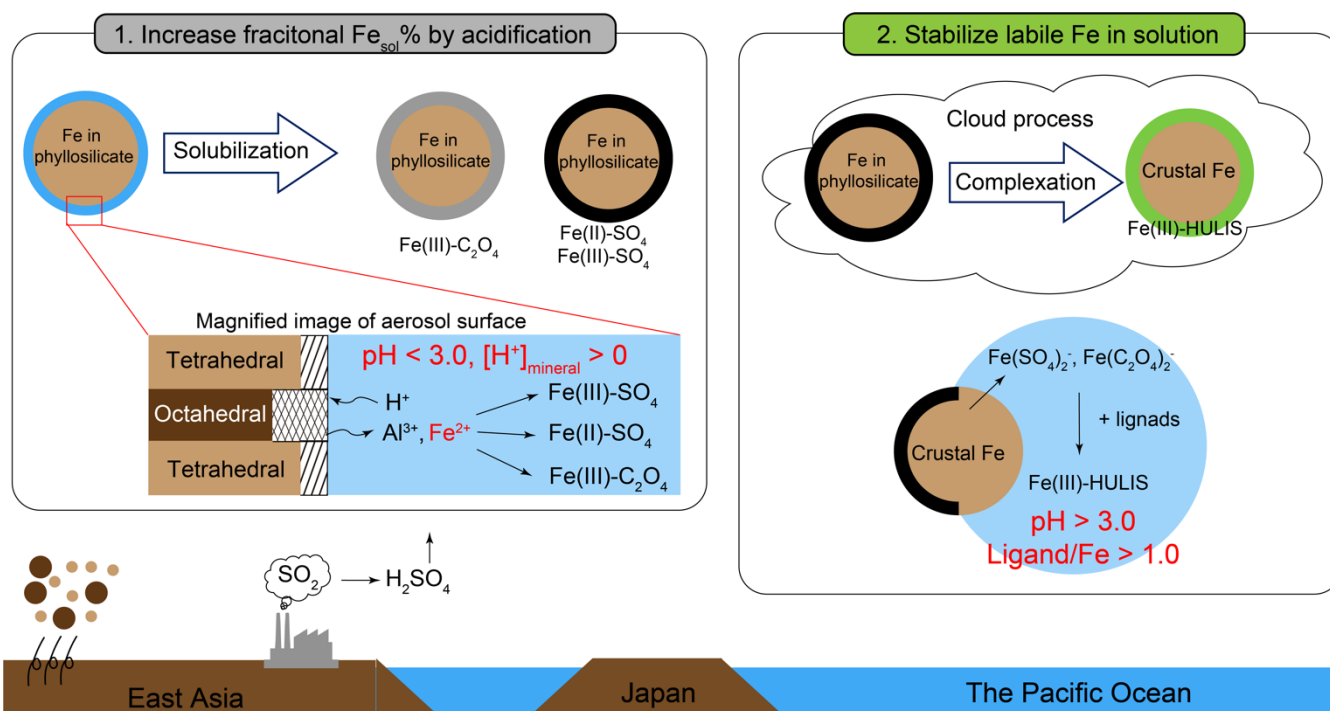
Table 1. Model parameter for three Fe-pool model.

	pH_{PPD}	Expected Fe species	%Fe(0)	Dissolution rate
Fast	1.0–2.0	Ferrihydrite Poor crystalline Fe-oxides	Fixed at 0.9	$\log k_{fast} = -0.50\, pH_{PPD} + 1.87$
	2.0–3.0		%FeT = $-0.4\, pH_{PPD} + 1.7$	
Intermediate	1.0–2.0	nano-size Fe-oxides	Fixed at 3.0	$\log k_{intermediate} = -0.66\, pH_{PPD} + 0.36$
	2.0–3.0		%FeT = $-2.0\, pH_{PPD} + 7.0$	
Slow	1.0–2.0	Crystalline Fe-oxides Fe in clay mineral	%FeT = $-15.2\, pH_{PPD} + 58.4$	$\log k'_{slow} = -0.44\, pH_{PPD} - 0.76$
	2.0–3.0			

630

References

Abualhaija, M. M., Whitby, H., and van den Berg, C. M. G.: Competition between copper and iron for humic ligands in estuarine waters, Mar. Chem., 172, 46–56, http://dx.doi.org/10.1016/j.marchem.2015.03.010, 2015.

635 Adachi, K., Oshima, N., Ohata, S., Yoshida, A., Moteki, N., and Koike, M.: Compositions and mixing states of aerosol particels by aircraft observations in the Arctic springtime, 2018, Atmos. Chem. Phys., 21, 3607–3626, https://doi.org/10.5194/acp-21-3607-2021, 2021.

Al-Abadleh, H. A.: Review of the bulk and surface chemistry of iron in atmospherically relevant systemns containing humic-like substances, RSC Adv., 5, 45785, https://doi.org/10.1039/C5RA03132J, 2015.

Angle, K. J., Crocker, D. R., Simpson, R. M. C., Mayer, J. J., Garofalo, L. A., Moore, A. N., Mora Garcia, S. L., Or, V. W.,

640 Srinivasan, S., Farhan, M., Sauer, J. S., Lee, C., Pothier, M. A., Farmer, D. K., Martz, T. R., Bertram, T. H., Cappa, C. D., Prather, K. A., and Grassian, V. H.: Acidity across the interface from the ocean surface to sea spray aerosol, Proc. Natl. Acad. Sci. U.S.A., 118, 2, e2018397118, https://doi.org/10.1073/pnas.2018397118, 2021.

Baker, A. R., and Jickells, T. D.: Mineral particle size as a control n aerosol iron solubility, Geophys. Res. Lett., 33, L17608, https://doi.org/10.1029/2006GL026557, 2006.

645 Baker, A. R., Kanakidou, M., Nenes, A., Myriokefalitakis, S., Croot, P. L., Duce, R. A., Gao, Y., Guieu, C., Ito, A., Jickells, T. D., Mahowald, N. M., Middag, R., Perron, M. M. G., Sarin, M. M., Shelley, R., and Turner, D. R.: Changing atmospheric acidity as a modulator of nutrient deposition and ocean biogeochemistry, Sci. Adv., 7, eabd8800, https://doi.org/10.1126/sciadv.abd8800, 2021.

Baker, A. R., Landing, W. M., Bucciarelli, E., Cheize, M., Fietz, S., Hayes, C. T., Kadko, D., Morton, P. L., Rogan, N., Sarthou,

650 G., Shelley, R. U., Shi, Z., Shiller, A., and van Hulten, M. M. P.: Trace element and isotope deposition across the air–sea interface: progress and research needs, Phil. Trans. R. Soc. A., 374, 20160190, http://dx.doi.org/10.1098/rsta.2016.0190, 2016.

Baker, A. R., Li, M., and Chance, R.: Trace metal fractional solubility in size-segregated aerosols from the tropical eastern Atlantic Ocean, Global Biogeochem. Cy. 34, e2019GB006510, https://doi.org/10.1029/2019GB006510, 2020.

Bethke, C. M.: Geochemical Reaction Modeling: Concepts and Applications. Oxford University Press, 1996.

655 Bibi, I., Singh, B., and Silvester, E.: Dissolution of illite in saline-acidic solutions at 25 ºC, Geochim. Cosmochim. Acta, 75, 3237–3249, https://doi.org/10.1016/j.gca.2011.03.022, 2011.

Bikkina, P., Kawamura, K., Bikkina, S., Kunwar, B., Tanaka, K., and Suzuki, K.: Hydroxy fatty acids in remote marine aerosols over the Pacific Ocean: Impact of biological activity and wind speed. ACS Earth Space Chem., 3, 366–379, https://doi.org/10.1021/acsearthspacechem.8b00161, 2019.

660 Bikkina, S., Kawamura, K., and Miyazaki, Y.: Latitudinal distributions of atmospheric dicarboxylic acids, oxocarboxylic acids and α-dicarbonyls over the western North Pacific: sources and formation pathways, J. Geophys. Res. Atmos. 120, 5010–5035. http://dx.doi.org/10.1002/2014JD022235, 2015.

Boris, A. J., Lee, T., Pari, T., Choi, J., Seo, S. J., and Collett Jr., J. L.: Fog composition at Baengnyeong Island in the eastern Yellow Sea: detecting markers of aqueous atmospheric oxidations, Atmos. Chem. Phys., 16, 437–453,
665   https://doi.org/10.5194/acp-16-437-2016, 2016.

Boyd, P. W., Jickells, T., Law, C. S., Blain, S., Boyle, E. A., Buesseler, K. O., Coale, K. H., Cullen, J. J., de Beear, H. J. W., Follows, M., Harvey, M., Lancelot, C., Levasseur, M., Owens, N. P. J., Pollard, R., Rivkin, R. B., Sarmiento, J., Schoemann, V., Smetacek, V., Takeda, S., Tsuda, A., Turner, S., and Watson, A. J.: Mesoscale iron enrichment experiments 1993–2005: Synthesis, and future directions, Science, 315, 612–617, https://doi.org/10.1126/science.1131669, 2007.

670   Bray, A. W., Oelkers, E. H., Bonneville, S., Wolff-Boenisch, D., Potts, N. J., Fones, G., and Benning, L. G.: The effect of pH, grain size, and organic ligands on biotite weathering rates, Geochim. Cosmochim. Acta, 164, 127–145, http://dx.doi.org/10.1016/j.gca.2015.04.048, 2015.

Buck, C. S., Landing, W. M., and Resing, J.: Pacific Ocean aerosols: Deposition and solubility of iron, aluminum, and other trace elements, Mar. Chem., 157, 117–130, http://dx.doi.org/10.1016/j.marchem.2013.09.005, 2013.

675   Buck, C. S., Landing, W. M., and Resing, J.: Particle size and aerosol iron solubility: A high-resolution analysis of Atlantic aerosols, Mar. Chem., 120, 14–24, https://doi.org/10.1016/j.marchem.2008.11.002, 2010.

Buck, C. S., Landing, W. M., Resing, J. A. and Lebon, G. T.: Aerosol iron and aluminum solubility in the northwest Pacific Ocean: Results from the 2002 IOC cruise, Geochem. Geophys. Geosyst., 7, 4, Q04M07, https://doi.org/10.1029/2005GC000977, 2006.

680   Chance, R., Jickells, T. D., and Baker, A. R.: Atmospheric trace metal concentrations, solubility and deposition fluxes in remote marine air over the south-east Atlantic. Mar. Chem., 177, 45–56, http://dx.doi.org/10.1016/j.marchem.2015.06.028, 2015.

Cheize, M., Sarthou, G., Croot, P. L., Bucciarelli, E., Baudoux, A. C., and Baker, A. R.: Iron organic speciation determination in rainwater using cathodic stripping voltammetry, Anal. Chim., Acta, 736, http://dx.doi.org/10.1016/j.aca.2012.05.011, 45–
685   54, 2012.

Chen, H., and Grassian, V. H.: Iron dissolution of dust source materials during simulated acidic processing: The effect of sulfuric, acetic, and oxalic acids, Envrion. Sci. Technol., 47, 10312–10321, https://doi.org/10.1021/es401285s, 2013.

Clegg, S. L., Pitzer, K. S., and Brimblecombe, P.: Thermodynamics of multicomponent, miscible, ionic solutions. II. Mixtures including unsymmetrical electrolyte. J. Phys. Chem., 96, 9470–9479, https://doi.org/10.1021/j100202a074, 1992.

690   Cohcran, R. E., Laskina, O., Hayarathne, T., Laskin, A., Laskin, J., Lin, P., Sultana, C., Lee, C., Moore, K. A., Cappa, C. D., Bertram, T. H., Prather, K. A., Grassian, V. H., and Stone, E. A.: Analysis of organic anionic surfactants in fine and coarse fractions of fershly emitted sea spray aeorsol, Environ. Sci. Technol., 50, 2477–2486, https://doi.org/10.1021/acs.est.5b04053, 2016.

Conway, T. M., Hamilton D. S., Shelley, R. U., Aguilar-Islas, A. M., Landing, W. M., Mahowald, N. ., and John, S. G.: Tracing
695   and constraining anthropogenic aerosol iron fluxes to the North Atlantic Ocean using iron isotopes, Nature Commun., 10, 2628, https://doi.org/10.1038/s41467-019-10457-w, 2019.

Cwiertny, D. M., Baltrusaitis, J., Hunter, G. J., Laskin, A., Scherer, M. M., and Grassian, V. H.: Characterization and acid-mobilization study of iron-containing mineral dust source materials. J. Geophys. Res. 113, D05202, https://doi.org/10.1029/2007JD009332, 2008.

700 Desboeufs, K. V., Losno, R., Vimeux, F., and Cholbi, S.: THe pH-dependent dissolution of wind-transported Saharan dust, J. Geophys. Res. Atmos., 104, D17, 21287–21299, https://doi.org/10.1029/1999JD900236, 1999.

Engelhart, G. J., Hildebrandt, L., Kostenidou, E., Mihalopoulos, N., Donahue, N. M., and Pandis, S. N.: Water content of aged aerosol, Atmos. Chem. Phys., 11, 911–920, https://doi.org/10.5194/acp-11-911-2011, 2011.

Fang, T., Guo, H., Zeng, L., Verma, V., Nenes, A., and Weber, R.: Highly Acidic Ambient Particles, Soluble Metals, and

705 Oxidative Potential: A Link between Sulfate and Aerosol Toxicity, Environ. Sci. Technol., 51, 2611–2620, https://doi.org/10.1021/acs.est.6b06151, 2017.

Fitzgerald, E., Ault, A. P., Zauscher, M. D., Mayol-Bracero, O. L., and Prather, K. A.: Comparison of the mixing state of long-range transported Asian and African mineral dust, Atmos. Environ., 115, 19–25, https://doi.org/10.1016/j.atmosenv.2015.04.031, 2015.

710 Friese, E., and Ebel, A.: Temperature dependent thermodynamic model of the system $H^+–NH_4^+–Na^+–SO_4^{2-}–NO_3^-–Cl^-–H_2O$. J. Phys. Chem. A, 114, 11595–11631, https://doi.org/10.1021/jp101041j, 2010.

Gledhill, M., and Buck, K. N.: The organic complexation of iron in the marine environment: a review. Front. Microbiol., 3, 69, https://doi.org/10.3389/fmicb.2012.00069, 2012.

Guo, H., Nenes, A., and Weber, R. J.: The underappreciated role of nonvolatile cations in aerosol ammonium-sulfate molar

715 ratios, Atmos. Chem. Phys., 18, 17307–17323, https://doi.org/10.5194/acp-18-17307-2018, 2018.

Hagvall, K., Persson, P., and Karlsson, T.: Speciation of aluminum in soils and stream waters: The impaortance of organic matter, Chem. Geol., 417, 32–43, http://dx.doi.org/10.1016/j.chemgeo.2015.09.012, 2015.

Hamilton, D. S., Scanza, R. A., Feng, Y., Guinness, J., Kok, J. F., Li, L., Liu, X., Rathod, S. D., Wan, J. S., Wu, M., and Mahowald, N. M.: Improved methodologies for Earth system modelling of atmospheric soluble iron and observation

720 comparisons using the Mechanism of Intermediate complexity for Modelling Iron (MIMI v1.0), Geosci. Model Dev., 12, 3835–3862, https://doi.org/10.5194/gmd-12-3835-2019, 2019.

Herrmann, H., Schaefer, T., Tilgner, A., Styler, S. A., Weller, C., Teich, M., and Otto, T.: Tropospheric aqueous-phase chemistry: Kinetics, mechanisms, and its coupling to changing gas phase, Chem. Rev., 115, 4259–4334, https://doi.org/10.1021/cr500447k, 2015.

725 Ildefonse, P., Cabaret, D., Sainctavit, P., Calas, G., Flank, A. M., and Lagarde, P.: Aluminum X-ray absorption near edge structure in model compounds and Earth's surface minerals, Phys. Chem. Minerals, 25, 112–121, https://doi.org/10.1007/s002690050093, 1998.

Ito, A., and Shi, Z.: Delivery of anthropogenic bioavailable iron from mineral dust and combustion aerosols to the ocean, Atmos. Chem. Phys., 16, 85–99, https://doi.org/10.5194/acp-16-85-2016, 2016.

730   Jeong, G. J., and Nousiainen, T.: TEM analysis of the internal structures and mineralogy of Asian dust particles and the
      implications for optical modeling, Atmos. Chem. Phys. 14, 7233–7254, https://doi.org/10.5194/acp-14-7233-2014, 2014.

      Jickells, T. D., An, Z. S., Andersen, K. K., Baker, A. R., Bergametti, G., Brooks, N., Cao, J. J., Boyd, P. W., Duce, R. A.,
      Hunter, K. A., Kawahata, H., Kubilay, N., laRoche, J., Liss, P. S., Mahowald, N., Prospero, J. M., Ridgwell, A. J., Tegen, I.,
      and Torres, R.: Global iron connections between desert dust, ocean biogeochemistry, and climate. Science, 308, 67–71,

735   https://doi.org/10.1126/science.1105959, 2005.

      Kawamura, K and Bikkina, S: A review of dicarboxylic acids and related compounds in atmospheric aerosols: Molecular
      distributions, sources, and transformation, Atmos. Res., 170, 140–160, http://dx.doi.org/10.1016/j.atmosres.2015.11.018, 2016

      Kim., H. J., Lee, T., Park, T., Park, G., Collett Jr., J. L., Park, K., Ahn, J. Y., Ban, J., Kang, S., Kim, K., Park, S. M., Jho, E.
      H., and Choi, Y.: Ship-borne observations of sea fog and rain chemistry over the North and South Pacific Ocean, J. Atmos.

740   Chem. 76, 315–326, https://doi.org/10.1007/s10874-020-09403-8, 2019.

      Kurisu, M., Adachi, K., Sakata, K., and Takahashi, Y.: Stable isotope ratios of combustion iron produced by evaporation in a
      steel plant, ACS Earth Space Chem., 3, 588–598, https://doi.org/10.1021/acsearthspacechem.8b00171, 2019.

      Kurisu, M., Sakata, K., Uematsu, M., Ito, A., and Takahashi, Y.: Contribution of combustion Fe in marine aerosols over the
      northwestern Pacific estimated by Fe stable isotope ratios, Atmos. Chem. Phys., 21, 16027–16050, https://doi.org/10.5194/acp-

745   21-16027-2021, 2021.

      Kurisu, M., Takahashi, Y., Iizuka, T., and Uematsu, M.: Very low isotope ratio of iron in fien aerosols related to its contribution
      to the surface ocean, J. Geophys. Res. Atmos., 121, 11119–11136, https://doi.org/10.1002/2016JD024957, 2016.

      Li, W., and Shao, L.: Transmission electron microscopy study of aerosol particles from the brown hazes in northern China, J.
      Geophys. Res. Atmos., 114, D09302, https://doi.org/10.1029/2008JD011285, 2009.

750   Li, W., Xu, L., Liu, X., Zhang, J., Lin, Y., Yao, X., Gao, H., Zhang, D., Chen, J., Wang, W., Harrison, R. M., Zhang, X., Shao,
      L., Fu, P., Nenes, A., and Shi, Z.: Air pollution-aerosol interactions produce more bioavailable iron for ocean ecosystems. Sci.
      Adv., 3, e1601749, https://doi.org/10.1126/sciadv.1601749, 2017.

      Longo, A. F., Feng, Y., Lai, B., Landing, W. M., Shelley, R. U.., Nenes, A., Mihalopoulos, N., Violaki, K., and Ingall, E. D.:
      Influence of atmopheric processes on the solubiility and composition of iron in Saharan dust, Environ. Sci. Technol., 50,

755   6912–6920, https://doi.org/10.1021/acs.est.6b02605, 2016.

      Mackie, D. S., Boyd, P. W., Hunter, K. A., and McTainhsh, G. H.: Simulating the cloud processing of iron in Australian dust:
      pH and dust concentration, Geophys. Res. Lett., 32, L06809, https://doi.org/10.1029/2004GL022122, 2005.

      Mahowald, N. M., Hamilton, D. S., Mackey, K. R. M., Moore, J. K., Baker, A. R., Scanza, R. A. and Zhang, Y.: Aerosol trace
      metal leaching and impacts on marine microorganisms, Nat. Commun., 9(1), 1–15, https://doi.org/10.1038/s41467-018-04970-

760   7, 2018.

      Martin, J. H., and Fitzwater, S. E.: Iron deficiency limits phytoplankton growth in the north-west Pacific subarctic, Nature,
      331, 341–343, https://doi.org/10.1126/science.1105959, 1988.

Maters, E. C., Delmelle, P., and Bonneville, S.: Atmospheric processing of volcanic glass: Effects on iron solubility and redox speciation, Envrion. Sci. Technol., 50, 5033–5040, https://doi.org/10.1021/acs.est.5b06281, 2016.

765 Matsuki, A., Iwasaka, Y., Shi, G., Zhang, D., Trochkine, D., Yamada, M., Kim, Y. S., Chen, B., Nagatani, T., Miyazawa, T., Nagatani, M., and Nakata, H.: Morphological and chemical modification of mineral dust: Observational insight into the heterogeneous uptake of acidic gases, Geophys. Res. Lett., 32, L22806, https://doi.org/10.1029/2005GL024176, 2005.

Mekhidze, N., Völker, C.: Al-Abadleh, H. A., Barbeau, K., Bressac, M., Buck, C., Bundy, R. M., Croot, P., Feng, Y., Ito, A., Johansen, A. M., Landing, W. M., Mao, J., Myriokefalitakis, S., Ohnemus, D., Pasquier, B., and Ye, Y.: Perspective on

770 identifying and characterizaing the process controlling iron speciation and residence time at the atmisohere-ocean interface, Mar. Chem., 217, 103704, https://doi.org/10.1016/j.marchem.2019.103704, 2019.

Meskhidze, N., Hurley, D., Royalty, T. M., and Johnson, M. S.: Potential effect of atmospheric dissolved organic carbon on the iron solubility in seawater, Mar. Chem., 194, 124–132, http://dx.doi.org/10.1016/j.marchem.2017.05.011, 2017.

Mochida, M., Kitamori, Y., and Kawamura, K.: Fatty acids in the marine atmosphere: Factors governing their concentrations

775 and evaluation of organic films on sea-salt particles, J. Geophys. Res., 107, D17, 4325, https://doi.org/10.1029/2001JD001278, 2002.

Moffet, R. C., Furutani, H., Rödel, T. C., Henn, T. R., Sprau, P. O., Laskin, A., Uematsu, M., and Gilles, M. K.: Iron speciation and mixing in single aerosols particles from the Asian continetal outflow, J. Geophys. Res., 117, D07204, https://doi.org/10.1029/2011JD016746, 2012.

780 Moore, C. M., Mills, M. M., Arrigo, K. R., Berman-Frank, I., Bopp, L., Boyd, P. W., Galbraith, E. D., Geider, R. J., Guieu, C., Jaccard, S. L., Jickells, T. D., La Roche, J., Lenton, T. M., Mahowald, N. M., Marañón, E., Marinov, I., Moore, J. K., Nakatsuka, T., Oschlies, A., Saito, M. A., Thingsted, T. F., Tsuda, A., and Ulloa, O.: Processes and patterns of oceanic nutrient limitation, Nature Geosci., 6, 701–710, https://doi.org/10.1038/ngeo1765, 2013.

Mori, I., Sun, Z., Ukachi, M., Nagano, K., McLeod, C. Q., Cox, A. G., Nishikawa, M.: Development and certification of the

785 new NIES CRM 28: urban aerosols for the determination of multielements, Anal. Bioanal. Chem., 391, 1997–2003, https://doi.org/10.1007/s00216-008-2076-y, 2008.

Nault, B. A., Campuzano-Jost, P., Day, D. A., Jo, D. S., Schroder, J. C., Allen, H. M., Bahreini, R., Bian, H, Blake, D. R., Chin, M., Clegg, S. L., Colarco, P. R., Crounse, J. D., Cubison, M. J., DeCarlo, P. F., Dibb, J. E., Diskin, G. S., Hodzic, A., Hu, W., Katich, J. M., Kim, M. J., Kodros, J. K., Kupc, A., Lopez-Hilfiker, F. D., Marais, E., Middlebrook, A. M., Neuman,

790 J. A., Nowak, J. B., Palm, B. B., Paulot, F., Pierce, J. R., Schill, G. P., Scheuer, E., Thornton, J. A., Tsigaridis, K., Wennberg, P. O., Willamson, C. J., and Jimenez, J. L.: Chemical transport models often underestimate inorganic aerosol acidity in remote regions of the atmosphere, Commun. Earth Environ., 2, 93, https://doi.org/10.1038/s43247-021-00164-0, 2021.

Nomura, M., and Koyama, A.: Performance of beamline with a pair of bent conical mirrors, Nucl. Instrum. Methods Phys. Res. A., 467–468, 733–736, https://doi.org/10.1016/S0168-9002(01)00482-X, 2001.

795 Nriagu, J. O., and Pacyna, J. M.: Quantitative assessment of worldwide contamination of air, water and soils by trace metals, Nature, 333, 134–139, https://doi.org/10.1038/333134a0, 1988.

Oakes, M., Weber, R. J., Lai, B., Russell, A., and Ingall, E.: Characterization of iron speciation in urban and rural single particles using XANES spectroscopy and micro X-ray fluorescence measurements: investigating the relationship between speciation and fractional iron solubility, Atmos. Chem. Phys., 12, 745–756, https://doi.org/10.5194/acp-12-745-2012, 2012.

800 Paris, R., and Desboeufs, K. V.: Effect of atmospheric organic complexation on iron-bearing dust solubility, Atmos. Chem. Phys., 13, 4895–4905, https://doi.org/10.5194/acp-13-4895-2013, 2013.

Paulot, F., Jacob, D. J., Johnson, M T., Bell, T. G., Baker, A. R., Keene, W. C., Lima, I. D., Doney, S. C., and Stock, C. A.: Global oceanic emission of ammonia: Constraints from seawater and atmospheric observations, Global Biogeochem. Cy., 29, 1165–1178, https://doi.org/10.1002/2015GB005106, 2015.

805 Prather, K. A., Bertram, T. H., Grassian, V. H., Deane, G. B., Stokes, M. D., DeMott, P. J., Aluwihare, L. I., Palenik, B. P., Azam, F., Seinfeld, J. H., Moffet, R. C., Molina, M. J., Cappa, C. D., Geiger, F. M., Roberts, G. C., Russell, L. M., Ault, A. P., Baltrusaitis, J., Collings, D. B., Corrigan, C. E., Cuadra-Rodriguez, L. A., Ebben, C. J., Forestieri, S. D., Guasco, T. J., Hersey, S. P., Kim, M. J., Lambert, W. F., Modini, R. L., Mui, W., Pedler, B. E., Ruppel, M. J., Ryder, O. S., Schoepp, N. G., Sullivan, R. C., and Zhao, D.: Bringing the ocean into the laboratory to probe the chemical complexity of sea spray aerosol.

810 Proc. Natl. Acad. Sci. U.S.A, 110, 7550–7555, https://doi.org/10.1073/pnas.1300262110, 2013.

Sakata, K., Kurisu, M., Tanimoto, H., Sakaguchi, A., Uematsu, M., Miyamoto, C., and Takahashi, Y.: Custom-made PTFE filters for ultra-clean size-fractionated aerosol sampling for trace metals, Mar. Chem., 206, 100–108, https://doi.org/10.1016/j.marchem.2018.09.009, 2018.

Sakata, K., Sakaguhci, A., Tanimizu, M., Takaku, Y., Yokoyama, Y., and Takahashi, Y.: Identification of sources of lead in
815 the atmosphere using X-ray absorption near-edge structure (XANES) spectroscopy, J. Environ. Sci., 26, 343–352, https://doi.org/10.1016/S1001-0742(13)60430-1, 2014.

Sakata, K., Takahashi, Y., Takano, S., Matsuki, A., Sakaguchi, A., Tanimoto, H.: First X-ray spectroscopic observations of atmospheric titanium species: size dependence and the emission source, Environ. Sci. Technol., 55, 10975–10986, https://doi.org/10.1021/acs.est.1c02000, 2021.

820 Sakata, M., Kurata, M., and Tanaka, N.: Estimating contribution from municipal solid waste incineration to trace metal concentrations in Japanese urban atmosphere using lead as a marker element, Geochem. J., 34, 23–32, https://doi.org/10.2343/geochemj.34.23, 2000.

Salazar, J. R., Pfotenhauer, D. J., Leresche, F., Rosario-Ortiz, F. L., Hannigan, M. P., Fakra, S. C., & Majestic, B. J.: Iron speciation in $PM_{2.5}$ from urban, agriculture, and mixed environments in Colorado, USA. Earth and Space Sci., 7,
825 e2020EA001262, https://doi.org/10.1029/2020EA001262, 2020.

Salma, I., and Láng, G. G.: How many carboxyl groups does an average molecule of humic-like sustances contain?, Atmos. Chem. Phys., 8, 5997–6002, https://doi.org/10.5194/acp-8-5997-2008, 2008.

Sambutoba, V., Didenko, T., Kunenkov, E., Emmenegger, C., Zenobi, R., and Kalbere, M.: Functional group analysis of high-molecular weight compounds in the water-soluble fraction of organic aerosols, Atmos. Environ., 41, 4703–4710,
830 https://doi.org/10.1016/j.atmosenv.2007.03.033, 2007.

Schlitzer, R.: Ocean Data View, odv.awi.de, 2021.

Schroth, A. W., Crusius, J., Sholkovitz, E. R., and Bostick, B. C.: Iron solubility driven by speciation in dust sources to the ocean, Nature Geosci., 2, 337–340, https://doi.org/10.1038/ngeo501, 2009.

Sedwick, P. N., Sholkovitz, E. R., and Chirch, T. M.: Impact of anthropogenic combustion emissions on the fractional solubility

835 of aerosol iron: Evidence from the Sargasso Sea, Geochem. Geophys. Geosyst., 8, 10, Q10Q06, https://doi.org/10.1029/2007GC001586, 2007.

Shah, V., Jacob, D. J., Moch, J. M., Wang, X., and Zhai, S.: Global modelling of cloud water acidity, precipitation acidity, and acid inputs to ecosystem, Atmos. Chem. Phys. 20, https://doi.org/10.5194/acp-20-12223-2020, 12223–12245, 2020.

Shaw, S. A., Peak, D., Hendry, M. J.: Investigation of acidic dissolution of mixed clays between pH 1.0 and -3.0 using Si and

840 Al X-ray absorption near edge structure, Geochim. Comochim. Acta, 73, 4151–4165, https://doi.org/10.1016/j.gca.2009.04.004, 2009.

Shi, Z., Bonneville, S., Krom, M. D., Carslaw, K. S., Jickells, T. D., Baker, A. R., and Benning, L. G.: Iron dissolution kineticks of mineral dust at low pH during simulated atmospheric processing, Atmos. Chem. Phys., 11, 995–1007, https://doi.org/10.5194/acp-11-995-2011, 2011.

845 Shi, Z., Krom, M. D., and Bonneville, S.: Formation of iron nanoparticles and increases in iron reactivity in mineral dust during simulated cloud processing, Envrion. Sci. Technol., 43, 6592–6596, https://doi.org/10.1021/es901294g, 2009.

Shi, Z., Krom, M. D., Bonneville, S., and Benning, L. G.: Atmospheric processing outside clouds increases solubile iron in mineral dust, Enciron. Sci. Technol., 49, 1472–1477, https://doi.org/10.1021/es504623x, 2015.

Sholkovitz, E. R., Sedwick, P. N., and Chrch, T. M.: Influence of anthropogenic combustion emissions on the deposition of

850 soluble aerosol iron to the ocean: Empirical estimates for island sites in the North Atlantic, Geochim. Csmochim. Acta, 73, 14, 3981–4003, https://doi.org/10.1016/j.gca.2009.04.029, 2009.

Spokes, L. Jickells, T. D., and Lim, B.: Solubilisation of aerosol trace metals by cloud processing: A laboratory study, Geichim. Cosmochim. Acta, 58, 15, 3281–3287, https://doi.org/10.1016/0016-7037(94)90056-6, 1994.

Stein, A. F., Draxler, R. R., Rolph, G. D., Stunder, B. J. B., Cohen, M. D. and Ngan, F.: Noaa's hysplit atmospheric transport

855 and dispersion modeling system, Bull. Am. Meteorol. Soc., 96(February), 2059–2077, https://doi.org/10.1175/BAMS-D-14-00110.1, 2015.

Sullivan, R. C., Guazzotti, S. A., Sodeman, D. A., and Prather, K. A.: Direct observations of the atmospheric processing of Asian mineral dust, Atmos. Chem. Phys., 7, 1213–1236, https://doi.org/10.5194/acp-7-1213-2007, 2007.

Sullivan, T. S., Ramkissoon, S., Garrison, V. H., Ramsubhag, A., and Thies, J. E.: Siderohore production of African dust

860 microorganisms over Trinidad and Tobago, Aerobiologia, 28, 391–401, https://doi.org/10.1007/s10453-011-9243-x, 2012.

Takahashi, Y., Furukawa, T., Kanai, Y., Uematsu, M., Zheng, G., and Marcus, M. A.: Seasonal changes in Fe species and soluble Fe concentration in the atmosphere in the Northwest Pacfic region based on the analysis of aerosols collected in Tsukuba, Japan, Atmos. Chem. Phys., 13, 7695–7710, https://doi.org/10.5194/acp-13-7695-2013, 2013.

Takahashi, Y., Higashi, M., Furukawa, T., and Mitsunobu, S.: Change of iron species and iron solubility in Asian dust during

865   the long-range transport from western China to Japan, Atmos. Chem. Phys., 11, 11237–11252, https://doi.org/10.5194/acp-11-11237-2011, 2011.

Takeichi, Y., Inami, N., Suga, H., Miyamoto, C., Ueno, T., Mases, K., Takahashi, Y., and Ono, K.: Design and performance of a compact scanning transmission X-ray microscope at the Photon Factory, Rev. Sci. Instrum., 87, 013704, http://dx.doi.org/10.1063/1.4940409, 2016.

870   Tao, Y., and Murphy, J. G.: The mechanisms responsible for the interactions among oxalate, pH and Fe dissolution in PM$_{2.5}$, ACS Earth Space Chem., 3, 2259–2265, https://doi.org/10.1021/acsearthspacechem.9b00172, 2019.

Taylor, S. R.: Abundance of chemical elements in the continental crust: a new table, https://doi.org/10.1016/0016-7037(64)90129-2, Geochim. Cosmochim. Acta, 28, 1273–1285, 1964.

Vinatier, V., Wirgot, N., Joly, M., Sancelme, M., Abrantes, M., Deguillaume, L., and Delort, A. M.: Sidreophore in cloud

875   waters and potential impact on atmospheric chemistry: Production by microorganisms isolated at the Puy de Dôme station, Environ. Sci. Technol., 50, 9315–9323, https://doi.org/10.1021/acs.est.6b02335, 2016.

Wang, Z., Fu, H., Zhang, L., Song, W., and Chen, J.: Ligand-promoted photoreductive dissolution of goethite by atmospheric low-molecular dicarboxylates, J. Phys. Chem. A, 121, 1647–1656, https://doi.org/10.1021/acs.jpca.6b09160, 2017.

Wilson, T. W., Ladino, L. A., Alpert, P. A., Breckels, M. N., Brooks, I. M., Browse, J., Burrows, S. M., Carslaw, K. S.,

880   Huffman, J. A., Judd, C., Kilthau, W. P., Mason, R. H., McFiggans, G., Miller, L. A., Nájera, J. J., Polishchuk, E., Rae, S., Schiller, C. L., Si, M., Temprado, J. V., Whale, T. F., Wong, J. P. S., Wurl, O., Yakobi-Hancock, J. D., Abbatt, J. P. D., Aller, J. Y., Bertram, A. K., Knopf, D. A., and Murray, B. J.: A marine biogenic source of atmospheric ice-nucleating particles, Nature, 525, 234–238, https://doi.org/10.1038/nature14986, 2015.

Wozniak, A. S., Shelley, R. U., McElhenie, S. D., Landing, W. M., and Hatcher, P. G.: Aerosol water soluble organic matter

885   characteristics over the North Atlantic Ocean: Implications for iron-binding ligands and iron solubility, Mar. Chem., 173, 162–172, http://dx.doi.org/10.1016/j.marchem.2014.11.002, 2015.

Wozniak, A. S., Shelley, R. U., Sleighter, R. L., Abdulla, H. A. N., Morton, P. L., Landing, W. M., and Hatcher, P. G.: Relationships among aerosol water soluble organic matter, iron and aluminum in European, North African, and marine air masses from the 2010 US GEOTRACES cruise, Mar. Chem., 154, 24–33, http://dx.doi.org/10.1016/j.marchem.2013.04.011,

890   2013.